Crystallization kinetics from Ge-rich Ge-Sb-Te thin films: influence of thickness

Philipp Hans[1§], Cristian Mocuta[2], Yannick Le-Friec[3], Philippe Boivin[4], Roberto Simola[4], Olivier Thomas[1]

[1] Aix Marseille Univ, Univ Toulon, CNRS, IM2NP UMR 7334, Marseille, France

[2] Synchrotron SOLEIL, L'Orme des Merisiers, Départementale 128, 91190 Saint-Aubin, France

[3] STMicroelectronics, 850 rue Jean Monnet, 38920 Crolles, France

[4] STMicroelectronics, 190 Ave Coq, 13106 Rousset, France

§Present Address: Synchrotron-Light for Experimental Science and Applications in the Middle East (SESAME), P.O. Box 7, Allan, 19252, Jordan

**Corresponding author*

Olivier Thomas (olivier.thomas@univ-amu.fr)

IM2NP UMR 7334 CNRS

Aix-Marseille Université

Faculté des Sciences, Campus de St Jérôme - Case 262

Avenue Escadrille Normandie Niemen

13397 Marseille Cedex 20

France

Abstract

The phase transition temperature and crystallization kinetics of Phase Change Materials (PCMs) are crucial characteristics for their performance, data retention and reliability in memory devices. Herein, the crystallization behavior and kinetics of a compositionally optimized, N-doped Ge-rich Ge-Sb-Te alloy (GGST) in the slow crystallization regime are systematically investigated using synchrotron X-ray diffraction (XRD) *in situ* during heat treatment. Uniform thin films (50, 25, 10 and 5 nm) of initially amorphous N-doped GGST are investigated. The specimens were heated up to 450 °C at a rate of 2 °C/min to estimate crystallization onsets by quantification of the crystallized quantity during material transformation from the XRD patterns. Subsequent isothermal anneals have been performed to assess crystallization behavior and activation energies. Nucleation-controlled crystallization that progresses in two steps is observed, together with the emergence of Ge preceding cubic $Ge_2Sb_2Te_5$, with a mild dependence of crystallization temperature on film thickness that is inverse to what has been observed in other systems. Ge and GST crystallization may be described occurring in three-time stages: (i) an incubation period; (ii) a fast growth period; (iii) a very slow growth period. Very high activation energies (between 3.5 and 4.3 eV) for each phase are found for the incubation time t_0. The activation energy for Ge in the fast growth regime is close to the one reported for the crystallization of pure Ge films. In the case of Ge, the incubation time is strongly thickness-dependent, which may have important consequences for the scaling of memories fabricated with this class of materials.

Introduction

Chalcogenide Ge-Sb-Te ternary alloys have attracted a lot of attention because of their capability to be switched reversibly between an amorphous and a crystalline phase [1-5]. The large contrast in physical properties (optical reflectivity, electrical conductivity…) between these two phases allow for an easy reading of the nature of the phase that has been induced either by furnace, laser or Joule heating. Moreover, this switching process can be very fast (in the range of 10s of ns), which opens avenues for memory applications that combine the high storage speed of dynamic random-access memory and the non-volatility of flash memory. Indeed, stand-alone applications have been reported [6] and Phase Change Materials (PCMs) are also considered for embedded memories since they are easily scalable and show good integration in back-end-of-line processes [7].

Many equilibrium phases have been reported in the Ge-Sb-Te ternary equilibrium diagram [8,9]. The ternary compound $Ge_2Sb_2Te_5$ (commonly named GST in the literature and thereafter in this article) has been particularly studied [9-12]. The stable structure of GST is trigonal (space group $P\bar{3}m1$) [13,14]. But, when crystallizing from an amorphous phase, GST crystallizes in a metastable cubic phase (space group $Fm\bar{3}m$) [14,15]. Crystallization from the amorphous phase remains the time-limiting process in phase-change based memories and a detailed understanding and modeling of the kinetics of crystallization of the PCM is critical. Many articles have been published on the kinetics of crystallization of GST [16-23]. These in-depth studies agree on a number of general features of the transformation in single phase GST that can be summarized as follows: (i) GST crystallizes at rather low temperatures, of the order of 140-150°C (compared with a melting temperature of 627°C and a glass transition temperature of 110°C); (ii) crystallization in GST is "nucleation-controlled" (This is the convention adopted by the PCM community, that names the controlling step as the fastest one. This is worth noting since an opposite convention is chosen by most phase transformation communities. For example, the community studying silicide formation by reactive diffusion between silicon and a metal film names a "nucleation-controlled reaction" [24] the situation when nucleation is the slowest step); (iii) at low annealing temperatures, i.e. at long crystallization times, the activation energy related to the crystallization of GST is of the order of 2.2-2.4 eV; (iv) at elevated annealing temperatures, i.e. above 300°C, a much smaller activation energy for crystallization [21-23] is observed (<1 eV). This is correlated with the

highly fragile [25] nature of GST with a very strong non-Arrhenius behavior of its viscosity (in the literature the fragility index m for GST goes from 20 to 140). These important findings clearly show how different crystallization kinetics can be in a real memory cell as compared to furnace anneals at reduced temperatures. These latter remain, however, an important prerequisite for understanding the crystallization process.

The crystallization temperature of GST is too low to satisfy the automotive market, that requires high-temperature data retention. Automotive applications require several years data retention at 150°C and five minutes at 260°C for soldering reflow. Ge-rich alloys have been shown to exhibit significantly higher crystallization temperatures [26] while preserving the switching speed. Compositionally optimized Ge-rich GST (named GGST thereafter) with a crystallization temperature above 350°C [27, 28] is thus an excellent candidate for embedded memory applications [29]. In addition, doping (C, Si, N, etc) is commonly used in PCMs as a tool to reduce mechanical stresses related to crystallization, increase crystallization temperature, or change the electrical resistance [30-33].

We have shown [34,35] in a previous work using synchrotron X-ray diffraction during furnace annealing (2°C/minute) of GGST thin films that crystallization of GGST occurs in two steps: pure Ge first crystallizes and this is followed by the crystallization of metastable cubic GST. This phase separation is expected since GGST composition does not correspond to a single crystalline phase and it has been observed by other authors [36], but it raises many questions about the complex kinetics at work and the length scales involved in this segregation. Interesting quantifications of the composition evolution in GGST memory cells [37] using electron spectroscopy allow for a detailed local analysis of the segregation process. Although it is borne to be different from what occurs at higher temperatures and crystallization speeds a systematic study of GGST crystallization kinetics in the slow crystallization regime is still missing.

It is the aim of the present article to investigate via *in situ* isothermal anneals and synchrotron X-ray diffraction the kinetics of crystallization of GGST thin films. Among different choices of doping elements nitrogen has been chosen here. In addition, we have studied the evolution of the kinetic parameters as a function of film thickness. From a fundamental point of view, it is interesting to evaluate the influence of confinement on phase transformation, but it is also very important for device scaling strategies.

Experimental

Thin film stacks have been prepared at STMicroelectronics with the following structure:
Si (001) substrate// 30 nm SiO2 / 75 nm SiN / x nm GGST (N-doped)/ 20 nm TiN / 25 nm SiN where x = 50, 25, 10 or 5. GGST layers were deposited by physical vapor deposition (PVD) followed by an *in situ* PVD TiN capping on an industrial tool. SiN capping was deposited by chemical vapor deposition (CVD). The capping layers ensure that the GGST films are protected against oxidation.

The X-ray diffraction (XRD) experiments have been performed on DiffAbs beamline [38] at Synchrotron SOLEIL (France). The samples were mounted inside an Anton Paar heater (model DHS 1100), allowing to precisely reach the desired annealing temperatures (within 1 deg.), while applying controlled heating ramps (from 1°C/min up to 300°C/min). An Aluminum home-made cylindrical dome, with 15 µm thick Kapton® windows was used to allow measuring the X-ray scattered signal from the sample with minimum X-ray absorption and parasitic scattering. During all the experiments, the sample was flushed using 99.999% purity (5n) N_2 gas. The heater was mounted on the 6-circle diffractometer (Kappa geometry) and the incident angle was maintained constant (10 degrees) during all the measurements.

The X-ray used were monochromatic, of energy 18 keV. The monochromaticity is ensured by a double crystal Si (111) monochromator (band pass $\Delta E/E \sim 10^{-4}$). Two 50 nm Rhodium coated Si single crystals mirrors ensure higher harmonics X-ray rejection of about 10^{-6}. The X-ray beam is focused in the vertical direction by longitudinally bent mirrors and in the horizontal direction by the sagittally bent second crystal of the monochromator. This results in a beam size (FWHM) of about 200 (V) × 250 (H) μm^2. The total photon flux in the spot is estimated to several 10^{11} ph/s at the chosen energy of 18 keV.

The XRD signal was acquired using an area detector (hybrid pixels, XPAD s140) [39-41], consisting of an array of 560 × 240 pixels (130 µm pitch) with no gaps. The detector was mounted on the detector circle of the diffractometer, thus allowing its positioning around the sample such to detect, into a single image / measurement, an angular range of about 11.0 × 4.1 ° ($2\theta \times \psi$, respectively the Bragg scattering angle and polar elevation). Depending on the sample thickness and the scattered signal to focus on, an XRD image was acquired every few to several 10s of seconds.

By knowing the exact positioning of the detector for each dataset, the pixel coordinates for each image are converted into angular coordinates, and then regrouped / averaged to obtain the 'classical' diffractograms (Intensity *vs.* 2θ datasets). More details about calibration, and data conversion into diffractograms can be found in [41,42].

The 1D-diffractograms were analyzed in two different ways. First, a purely numerical integration procedure was applied to extract the intensities only. That procedure consists of i) data smoothing with a Savitzky-Golay filter; ii) averaging of the first 10 patterns (typically acquired at room temperature, i.e. for amorphous GGST films) to use them as a background; iii) subtracting that average from all following patterns; iv) fitting a linear background in windows around the peaks of interest and subtracting that linear background to account for possible negative intensities and offsets, which are expected at crystallization (the diffuse scattering originating from the amorphous GGST layer will diminish when the layer crystallizes); v) integrating the area under the curve by summing the intensities. This method is very fast, although potential downsides might be that the areas are only obtained by numerical integration, whereas maxima potentially could consist of overlapping peaks.

To analyze the breadth and position of the diffraction peaks, fitting with a Voigt profile was also implemented [35].

Results

Phase identification in crystallized samples

All the as deposited films are amorphous as evidenced by their diffraction patterns (Figure 1) but diffraction peaks appear after annealing up to 450°C. The following peaks can be indexed (Figure 1) in the investigated angular range: c-GST 111, Ge **111**, c-GST **200** (this diffraction peak may be superimposed with trigonal-GST 013 which gives rise to a shoulder on the low-angle side), Ge **220**, c-GST **220,** where trigonal-GST and c-GST stand respectively for trigonal and cubic GST.

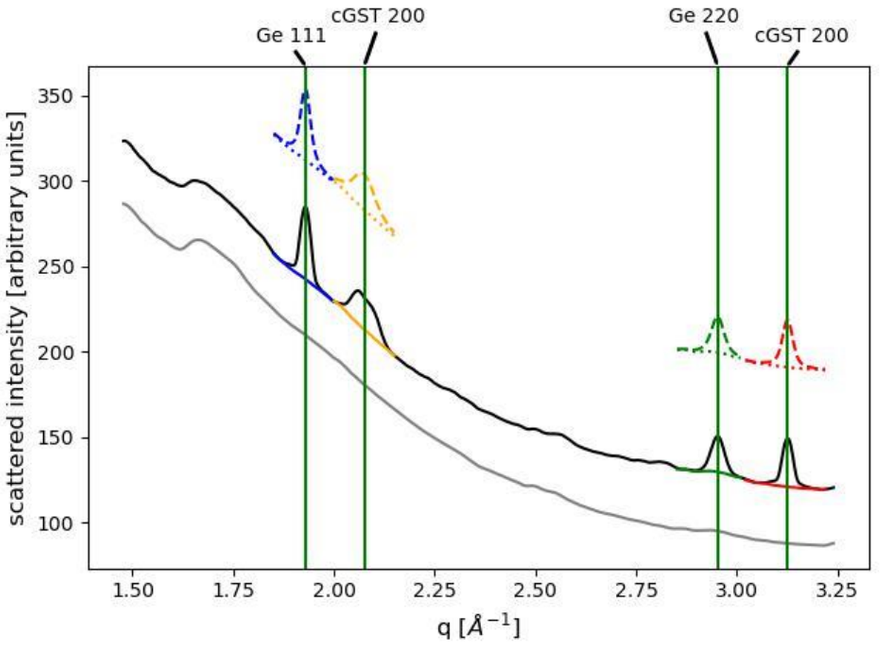

Fig. 1: Diffraction patterns from a 50 nm GGST film as deposited and after annealing (2°C/minute) up to 450°C. The background that was obtained by averaging ten room temperature patterns of the pristine state (grey) is vertically shifted for clarity from the XRD pattern of the corresponding crystallized thin film. The fitted peaks and corresponding local backgrounds are plotted colored, with dashed lines. Green vertical lines indicate the names of the identified X-ray reflections.

Ramp anneals: estimating crystallization temperature

Ramp anneals (2°C/minute) under N_2-atmosphere were performed up to 450°C on all samples. Figure 2 shows the evolution of integrated intensity for Ge 111 and cubic GST 200 as a function of temperature for different film thickness. Intensities have been normalized to the incoming intensity I_0 and corrected for the beam footprint (as related to the incident angle), but not normalized with the film thickness – this explains the various intensity plateaus reached when cooling down. One observes that Ge crystallization occurs before GST crystallization, in agreement with previous studies [34-36], with a temperature difference of about 3°C (see table 1). The crystallization temperatures (T_x) for both phases are reported in table 1. They have been determined using linear fits on smoothed data (Savitzky-Golay filter). A mild increase in the crystallization temperature is observed when decreasing film thickness. The very weak signal over background ratio from the 5 nm film made the extraction of integrated intensity and thus crystallization temperature too unreliable to be reported here.

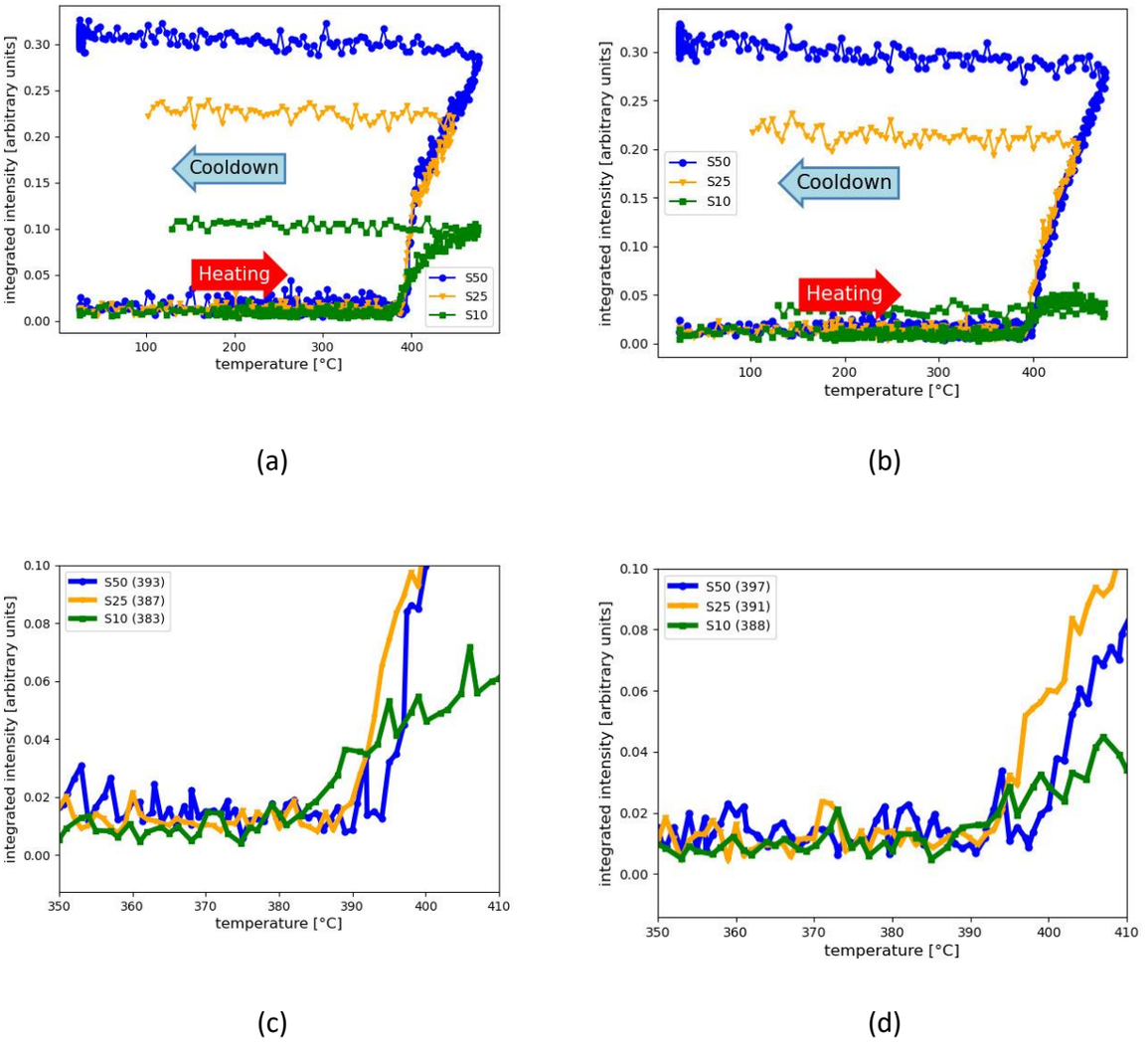

Fig. 2: Integrated intensities from (a) Ge **111** and (b) GST **200** during ramp anneals (2°C/min) of GGST films of varying thickness: for a film thickness of 50 nm (circles), 25 nm (triangles), and 10 nm (squares). (c) and (d) show a magnified view of the temperature interval when crystallization sets.

Film thickness (nm)	T_x Ge (°C)	T_x GST (°C)
10	378± 6	385± 5
25	388± 3	391± 2
50	392± 4	396± 3

Table 1: Crystallization temperatures (T_x) for Ge and cubic GST in GGST thin films as deduced from the evolution of numerically integrated diffraction intensities vs temperature at a heating rate of 2°C/minute.

Isothermal anneals

Isothermal anneals have been performed using the following procedure: (i) the heater is sent to the target temperature with maximum ramp rate (300°C/minute nominally but closer to 275°C/minute according to our measurements); (ii) the target temperature is typically reached within max 2 minutes, taking into account the 30-50 s lag before heating is actually initiated. This lag time is not considered, and in all the following treatments t=0 is taken as the time when temperature has reached 95% of target temperature.

In situ XRD isothermal anneals have been performed at different temperatures above and below the crystallization temperatures derived from 2°C/minute ramp anneals (Table 1). A typical evolution for the Ge **111** and GST **200** integrated intensities is shown in Figure 3 for the 50 nm thick GGST sample. One can distinguish three regimes that will be named I, II and III in the following.

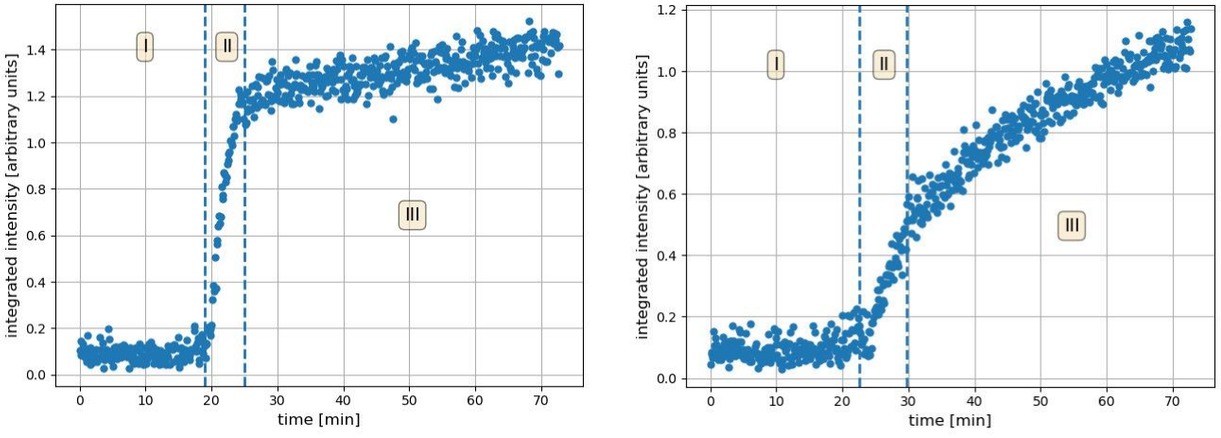

(a) (b)

Fig. 3: Evolution of (a) Ge **111** and (b) GST **200** integrated intensities as a function of time for a 50 nm GGST film at constant temperature (385°C).

Regime I corresponds to an "incubation time" during which no crystalline phase is detected. Regime II corresponds to a first fast growth regime and regime III corresponds to a slow growth stage. This three-stages behavior has been observed for all the investigated thickness excepting the 5 nm case where the signal to noise ratio is too low for getting meaningful results. Consequently the 5 nm film is not considered in the following analysis.

Modeling tests based on the classical Johnson-Mehl-Avrami-Kolmogorov [43-47] or derivations from it [48-50] failed to reproduce correctly this three-stages behavior and yielded unphysical Avrami exponents (larger than 10). We chose instead a more modest approach aimed at determining the three characteristic times and monitoring their temperature behavior. Consequently, to extract the characteristic times (t_0: incubation time, t_1: fast growth regime, t_2: slow growth regime) for these three stages we have used a phenomenological fitting of integrated intensity vs time:

$$For\ t \le t_0\ \ I(t) = \left(\frac{I_{max} - I_0}{2}\right) tanh\left[\frac{t - t_0}{t_1}\right] + \frac{I_{max} + I_0}{2} \quad (1)$$

$$For\ t \ge t_0\ \ I(t) = \left(\frac{I_{max} - I_0}{2}\right) tanh\left[\frac{t - t_0}{t_1}\right] + \frac{I_{max} + I_0}{2} + \frac{t - t_0}{t_2}$$

Where I_{max}, I_0, t_0, t_1 and t_2 are fitting parameters. The corresponding fits are shown in figure 4 for all temperatures. A reasonably good fit is obtained at all temperatures, which allows extracting the characteristic times for each stage and each phase at different temperatures. Similar plots are obtained for 25 nm and 10 nm film thickness and are shown in SuppL. Materials figures S1, S2and S3.

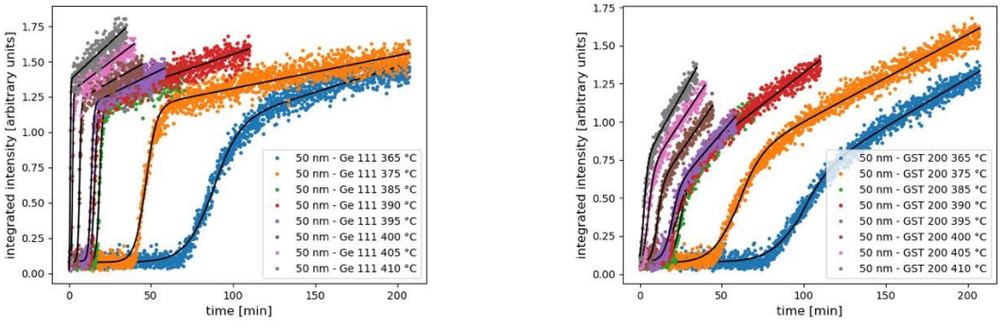

(a) (b)

Fig. 4: (a) Evolution of Ge **111** integrated intensity as a function of time for a 50 nm GGST film at constant temperature (365 to 410°C). (b) Same plot for GST **200**.

The times t_0, t_1 and t_2 are presented for Ge **111** and GST **200** and for different film thickness respectively in figures 5 (t_0), 6 (t_1) and 7 (t_2) in an Arrhenius representation. Activation energies extracted from linear fits are given in table 2.

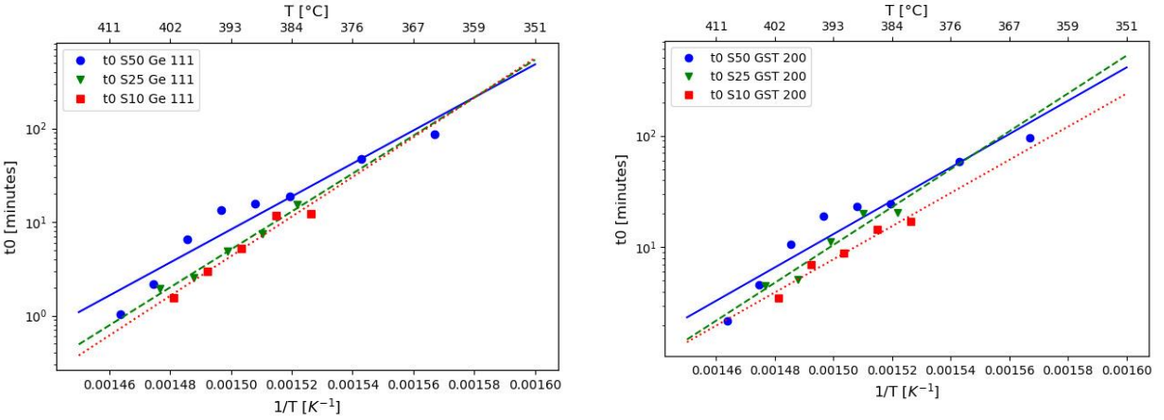

(a) (b)

Fig. 5: Incubation time t_0 plotted in an Arrhenius representation for Ge **111** (a) and GST **200** (b) for a film thickness of 50 nm (circles), 25 nm (triangles) and 10 nm (squares). Lines are linear fits to the data.

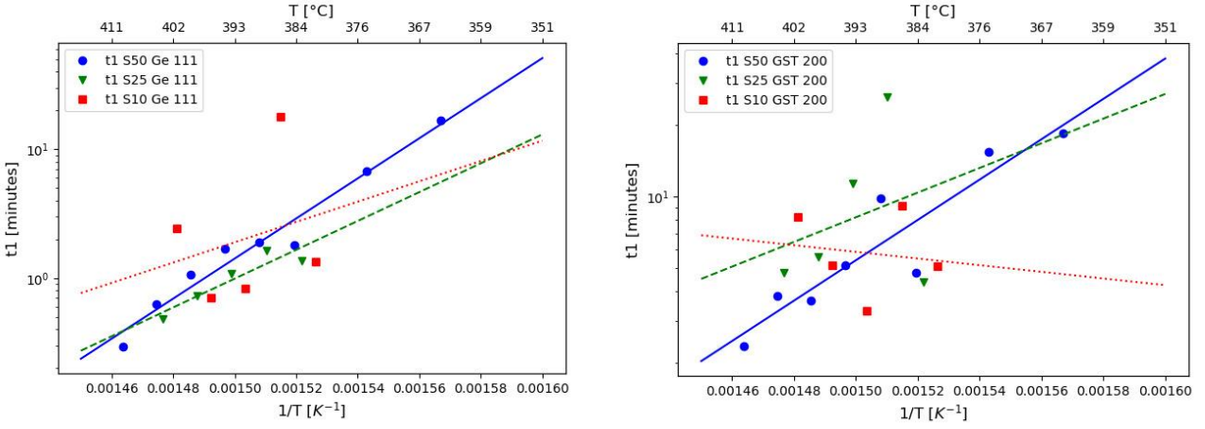

(a) (b)

Fig. 6: Growth time t_1 plotted in an Arrhenius representation for Ge **111** (a) and GST **200** (b) for a film thickness of 50 nm (circles), 25 nm (triangles) and 10 nm (squares). Lines are linear fits to the data.

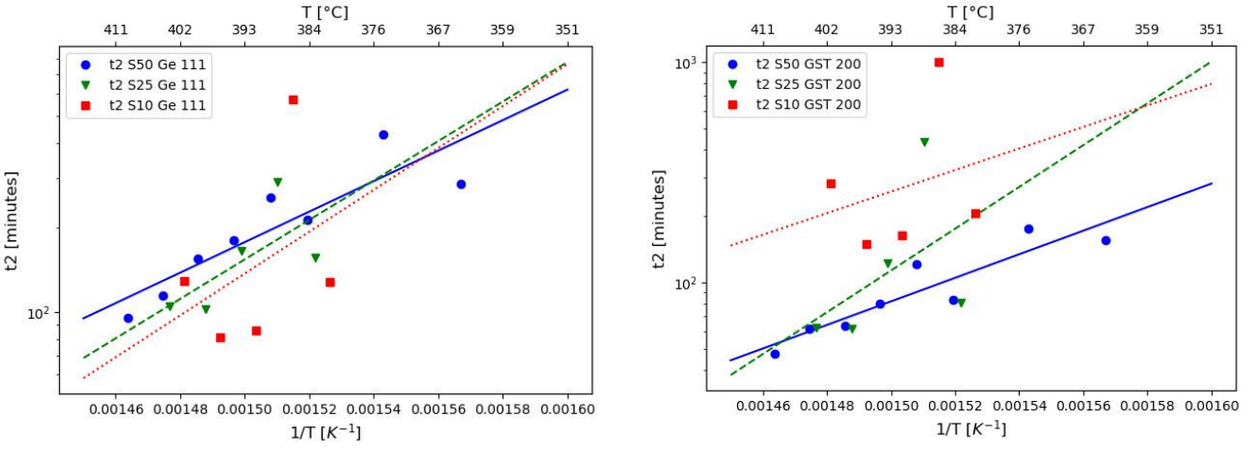

(a) (b)

Fig. 7: Time t_2 plotted in an Arrhenius representation for Ge **111** (a) and GST **200** (b) for a film thickness of 50 nm (circles), 25 nm (triangles) and 10 nm (squares). Lines are linear fits to the data.

	Thickness (nm)	Activation energy Ge (eV)	Activation energy GST (eV)
t_0	50	3.6 ± 0.2	3.0 ± 0.2
	25	4.0 ± 0.1	3.3 ± 0.3
	10	4.3 ± 0.3	3.0 ± 0.2
t_1	50	3.1 ± 0.1	1.6 ± 0.1
	25	2.2 ± 0.3	0.9 ± 1.0
	10	1.6 ± 1.8	-0.3 ± 0.6
t_2	50	1.0 ± 0.1	1.0 ± 0.1
	25	1.3 ± 0.4	1.8 ± 0.9
	10	1.2 ± 1.0	0.9 ± 1.0

Table 2: Activation energies derived from a linear regression of Arrhenius plots shown in Figures 5, 6 and 7. Grayed values correspond to cases where high scatter of values removes any significance to the obtained activation energy.

Similar results are obtained for Ge **220** and GST **220** diffraction peaks and are reported in Suppl. Material table S1 and figure S4.

The incubation time t_0 clearly follows an Arrhenius behavior with a high activation energy which is of the order of 4 eV for Ge and 3 eV for GST. In the case of Ge crystallization this activation energy increases significantly from 3.6 eV to 4.3 eV when the film thickness decreases from 50 to 10 nm.

The rapid-growth time t_1 exhibits an Arrhenius behavior for the 50 nm film thickness which is of the order of 3.1 eV for Ge and 1.6 eV for GST. For smaller film thickness a large scatter in the extracted values makes difficult drawing any significant trend especially in the case of the weak GST **200** diffraction peak. There is, however, a decrease in activation energy for Ge growth when thickness decreases.

The slow-growth characteristic time t_2 shows a lot of scatter when plotted as a function of temperature. It seems that this slow growth regime is not temperature-dependent (at least in the range of investigated temperatures) as evidenced by the evolution of integrated intensities (Figure 4, S1, S2 and S3).

Fitting the diffraction peaks with a Voigt profile allowed to extract the evolution of d-spacing and integral breadth Δq of Ge **111, Ge 220**, GST **200** and GST **220** peaks as a function of time during isothermal annealing. Figure 8 and 9 show the evolution of respectively d-spacings and Δq of Ge **111, Ge 220**, GST **200** and GST **220** peaks for different temperatures as a function of time for a film thickness of 50 nm (where the main figure shows their evolutions over the complete measurement range, whereas insets are displayed on the same ranges as the fits of regimes I, II and III, such as in figure 4). From the d-spacing evolution of Ge **111** and Ge **220** one can observe a small positive strain variation of the order of 0.1 %, followed by a slow decrease at long annealing times. The evolutions of the GST **200** and **220** peaks appear completely opposite: GST **200** d-spacing increases steadily whereas GST **220** d-spacing increases, levels off and then decreases for very long annealing times. The surprising increase in GST **200** d-spacing is caused by the single peak fitting and the appearance of trigonal-GST **013** that displaces the peak towards larger distances. In the same way the integral breadth of GST **200** (Figure 9.c) increases as a function of time because of the additional diffraction peak from trigonal-GST. The GST **220** d-spacing initial increase is highest for the higher temperatures and reaches up to 0.1 % positive strain. The very slow evolution at long annealing times appears as a relaxation of this initial strain. The Bragg angles for Ge **111** and Ge **220**, at 18 keV are about 6.05° and 9.91° which indicates that at 10° incidence one is probing corresponding planes with an inclination with respect to surface normal of respectively 4° and 0.09°. Considering that strain varies roughly with the square of the sine of this inclination angle one can state with a good approximation that the probed strain is the strain normal to the surface.

The integral breadth Δq of Ge **111** and **220** decreases as a function of time. Since the breadth of the two peaks are close the main contribution to this parameter is size broadening. The initial value of 0.065 $Å^{-1}$ (for Ge **220**) translates into a mean crystallite size of about 10 nm (using $\Delta q = 2\pi / D$, where Δq is the integral breadth and D is crystallite size). For very long annealing times the integral breadth reaches 0.03 $Å^{-1}$ which corresponds to a mean crystallite size of 21 nm. Values extracted from either Ge **220** or Ge **111** are close, indicating a weak contribution from microstrains to the integral breadth. The integral breadth of GST **220** decreases continuously as a function of time and indicates a crystallite size evolving from 21 nm to 29 nm.

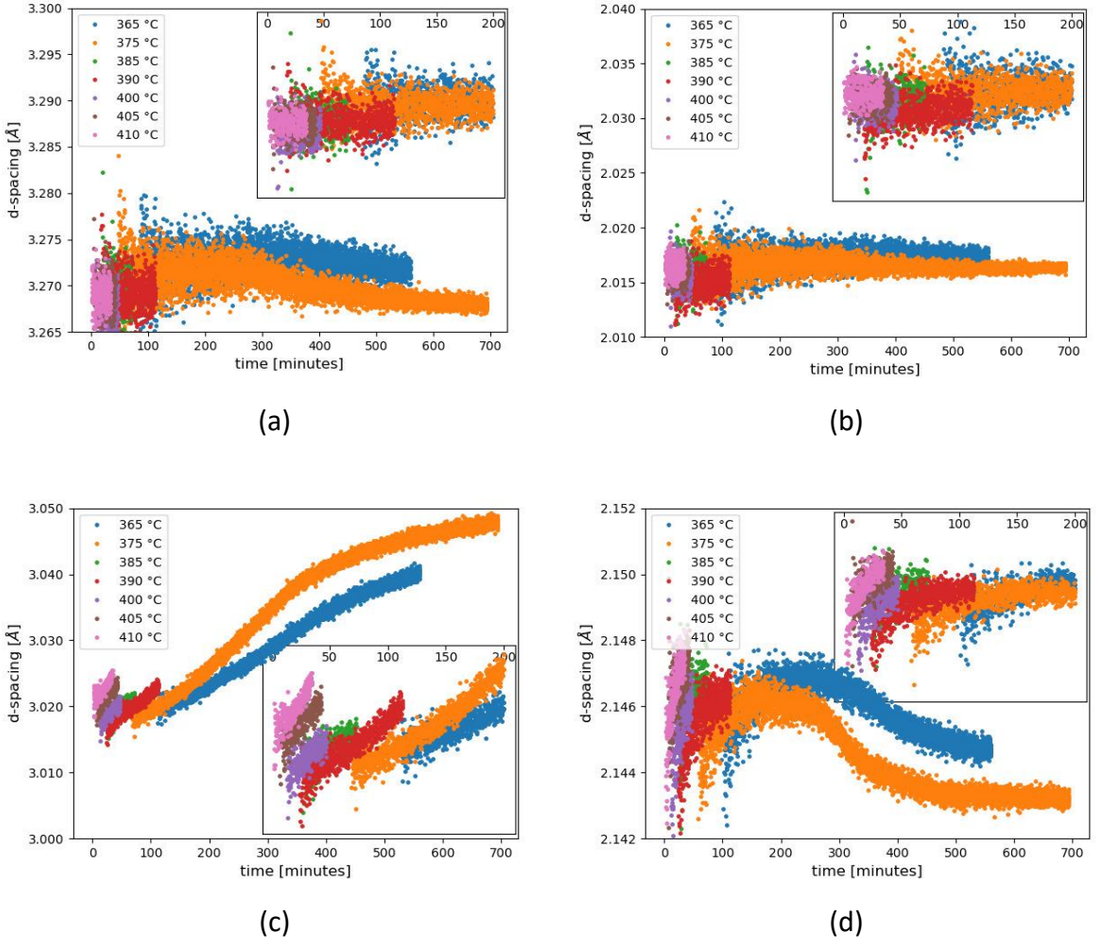

Fig. 8: Evolution of d-spacing for Ge **111** (a), **Ge 220** (b), GST **200** (c) and GST **220** (d) peaks as a function of time at different temperatures for 50 nm GGST sample. Insets are zooms of the first 200 min. of the annealing time. As discussed in the text the surprising increase in GST 200 d-spacing is caused by the single peak fitting and the appearance of trigonal-GST 013 that

displaces the peak towards larger distances. In the same way the integral breadth of GST 200 (Figure 9.c) increases as a function of time because of the additional diffraction peak from trigonal-GST.

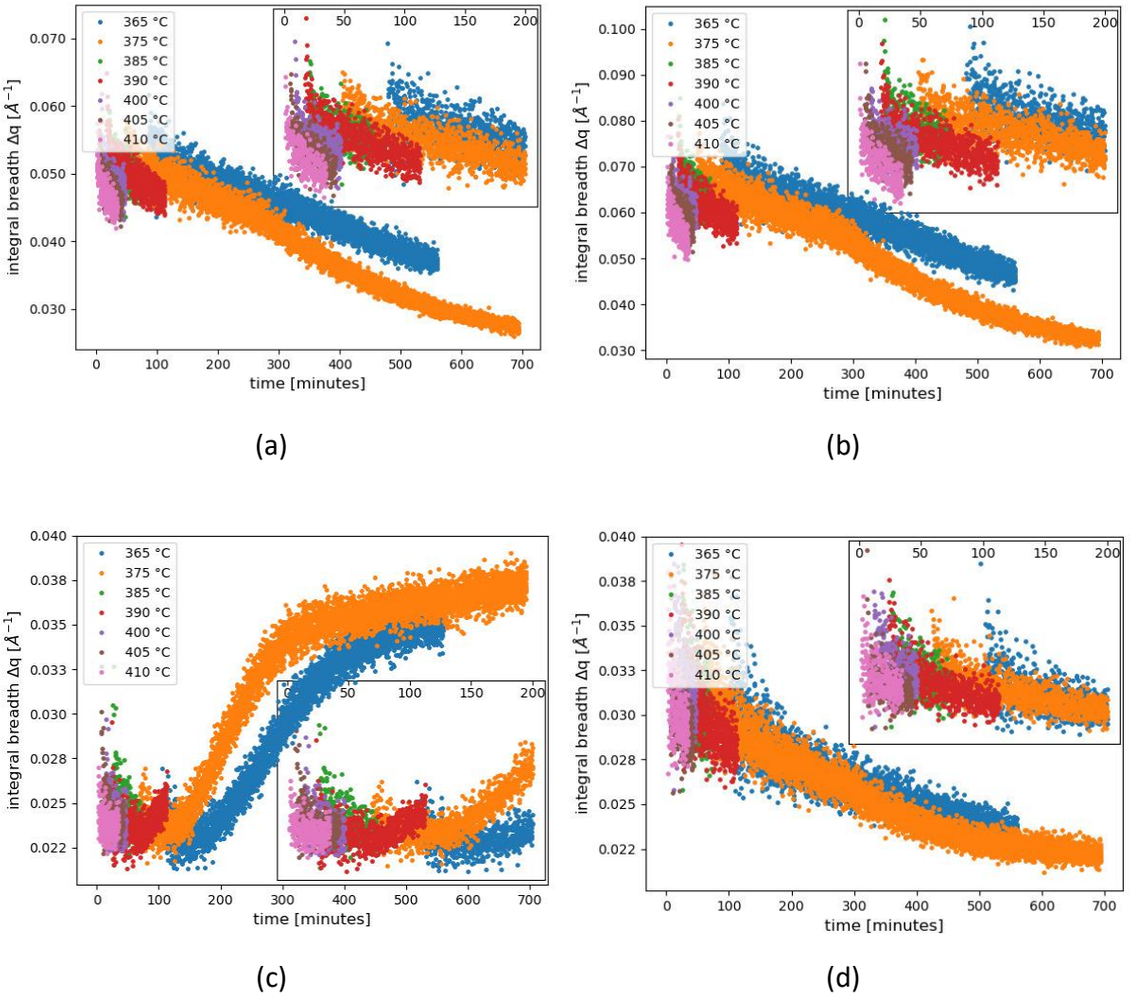

Fig. 9: Evolution of integral breadth for Ge **111** (a), **Ge 220** (b), GST **200** (c) and GST **220** (d) peaks as a function of time at different temperatures for 50 nm GGST sample. Insets are zooms of the first 200 min. of the annealing time. As discussed in the text the integral breadth of GST 200 (Figure 9.c) increases as a function of time because of the additional diffraction peak from trigonal-GST.

Discussion

In agreement with previous investigations [33-35] we observe a crystallization process of Ge-rich N-doped GST films of thickness ranging between 50 and 5 nm occurring in two steps where Ge crystallization precedes cubic GST crystallization (either in temperature during ramp anneals or in time during isothermal anneals). During a 2°C/minute anneal Ge crystallizes at about 385°C followed by GST crystallization at about 389°C. These crystallization temperatures are only weakly dependent on film thickness. This behavior is very different from what has been observed in pure phase systems. Exponential increase in crystallization temperature as a function of decreasing thickness has been reported for Ge [51-53], GeTe [54] and GST [55, 56]. In Zacharias' model [57] this dependence has been interpreted in the framework of nucleation theory.

Monitoring of X-ray diffraction during isothermal annealing of GGST thin films has allowed us evidencing crystallization in three stages: during stage I (total length t_0) no diffraction signal is detectable. Thus, the sample appears to remain amorphous. After time t_0 ("incubation time") Ge crystallizes followed by a delayed crystallization of the GST cubic phase. A first fast growth regime (characteristic time t_1) is followed by a much slower one (characteristic time t_2).

The phase separation of the Ge-rich amorphous film first into the Ge diamond structure-phase followed by GST cubic metastable phase has been reported by several authors [34-36]. This phase separation requires Ge atoms to be mobile and the formation of nano-sized clusters in the amorphous phase prior to Ge crystallization has been observed by Transmission electron Microscopy [36,37]. One may thus wonder whether the limiting step for crystallization in GGST is the diffusion of elements in the amorphous matrix (here: the one of Ge since it is the major species in the amorphous alloy). The self-diffusion of Ge in the amorphous and in the crystalline phases has been studied by Hüger *et al.* [58]. They found that Ge diffusivity is orders of magnitude faster in the amorphous phase (activation energy 2.11 eV, pre-exponential factor 6.2 X 10^{-6} m^2 s^{-1}) as compared to the crystalline phase (activation energy 3.13 eV). The activation energy for the incubation time found in this work is significantly higher (between 3.5 and 4.3 eV depending on the film thickness) than the activation energy for Ge diffusion. Such a high activation energy points rather to a nucleation barrier. Ge crystallization from amorphous Ge films has been studied by several authors [51-

53, 59, 60]. Ge films are reported to crystallize between 425°C and 500°C with an activation energy of 2.96 eV [59]. Hence the crystallization temperature of Ge in GGST is lower than the one of pure Ge and crystallization time t_0 of GGST has a significantly higher activation energy than the one of pure Ge. In the temperature range investigated in the present work, the Ge diffusion length for diffusion of Ge in amorphous Ge is of the order of 1 nm. This size probably easily permits the formation of critical nuclei and thus the crystallization process might be controlled by the nucleation barrier (hence the high activation barrier). This high activation energy might also be related to the high fragility index of the surrounding amorphous GST matrix [19] (Fragility, as defined by Angell [25] characterizes the non-Arrhenius behavior of the viscosity in the glass phase). It is worth noting that GST crystallization in the GGST amorphous mixture is delayed to much higher temperatures as compared to pure GST. The activation energy for GST incubation time found in the present work is of the order of 3 eV, significantly higher than the activation energy reported for crystallization of pure GST [16-23] thin films (2.2-2.4 eV). This difference may be caused by the need to continuously expel extra germanium atoms from Ge-rich areas. Finally, it is worth emphasizing that the activation energy for Ge crystallization incubation time is strongly thickness-dependent (see figure 10) with a higher activation energy at smaller thickness. This cannot be explained by the variation of interfacial energy involved in the nuclei formation as is suggested by the Zacharias model [57]. Zacharias and Streitenberger model is a thermodynamic model based on classical nucleation theory, where the free energy of a crystalline nucleus is written as the sum of a volumetric term (the difference in free energies per unit volume between the crystalline and amorphous phases times the volume of the nucleus) and a surface/interface term, which is simply the total surface energy of the nucleus. In an ultra-thin film the upper and lower interfaces are getting close to the upper and under-layers and Zacharias and Streitenberger [57] propose an interface energy that varies exponentially with the nucleus-interface distance. The minimization of the Gibbs free energy of the nucleus yields then an activation barrier that decreases exponentially with film thickness, which is not what is observed in the present experiments. As for the evolution of crystallization temperature with film thickness the behavior of GGST thin films is very different from common behavior (GST or Ge films). A possible explanation is that Ge crystallization occurs in localized Ge-rich areas controlled by elemental diffusion in the amorphous matrix. For very thin films the size of these areas becomes limited by the film thickness. Nucleation in confined media has been studied by

Kwon et al. [61] by phase field modeling. They have shown that in confined media JMAK kinetics break down and growth of crystalline phase occurs in Single Nucleus Crystallization regime, which results in a much slower crystallization rate.

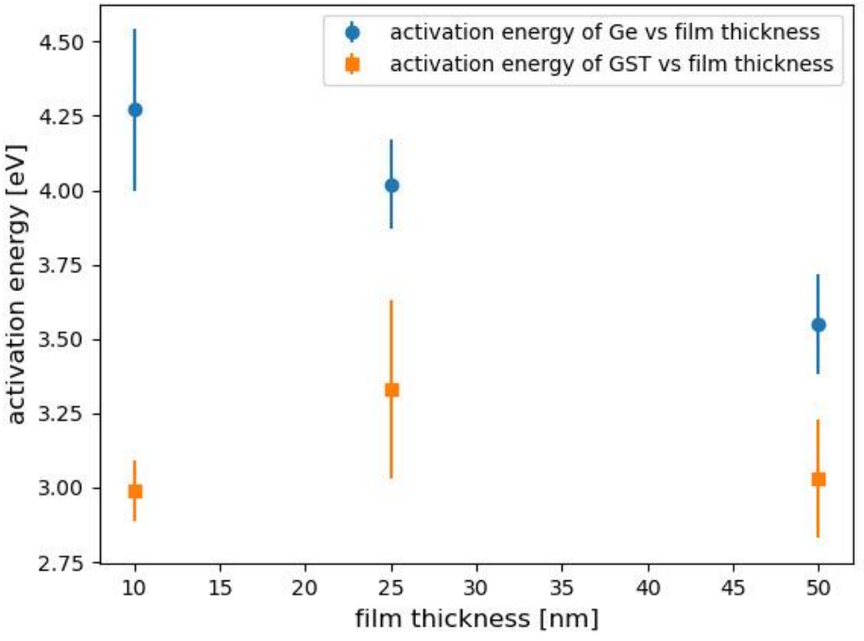

Fig. 10: Activation energy of incubation time for Ge (blue filled circles) and for GST (orange filled squares) as a function of film thickness.

The interpretation that Stage I is related to the nucleation step of Ge crystallites is supported by the striking influence of an underlayer on the crystallization of GGST. Figure 11 shows a comparison between the crystallization of a 50 nm GGST film on SiN (as in Figure 3.a) and the crystallization of a 45 nm GGST film on a 5 nm underlayer with composition Ge:Sb:Te derived from 2:2:5. The presence of the underlayer completely suppresses the incubation stage, probably acting as a nucleation seed.

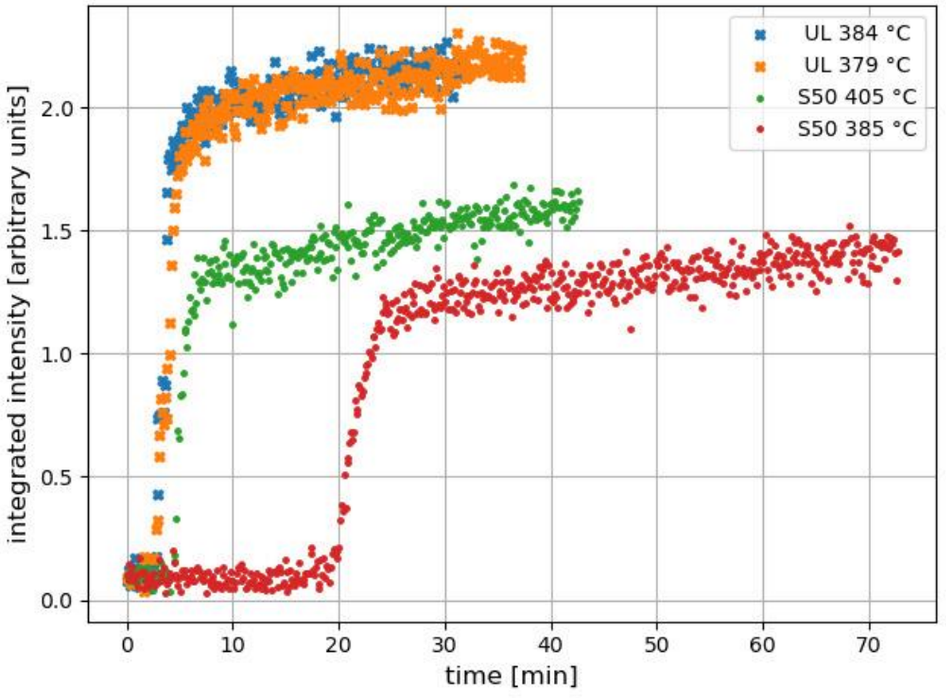

Fig. 11: Evolution of Ge **111** integrated intensity as a function of time at constant temperature for a 50 nm GGST film (S50) and for a 5 nm UL/45 nm GGST stack (UL).

The activation energy for the growth of Ge or GST in 50 nm GGST thin films (stage II) is respectively 3.0 and 1.6 eV. These energies may be related to growth of crystallites and thus diffusion of relevant species from the surrounding matrix to the growing crystal. One notes that 3.0 eV is close to the activation energy (2.96 eV) reported for the crystallization of amorphous Ge films [50].

The slow continuous increase of diffracted intensity (stage III) after this growth stage is puzzling. This trend has been observed in all the experiments we have performed on various GGST films. It indicates that there remains a small portion of amorphous material that slowly crystallizes. In a low temperature isothermal anneal increasing the temperature after some time (see figure S5 in Supplementary material) triggers an increase in the diffracted intensity, which indicates indeed that additional material has been crystallized.

Finally, it is important to emphasize that these findings have important consequences for the scaling of memory devices. We have shown that, in simple thin film structures, film thickness has a very large influence on crystallization kinetics. One should expect even larger effects for more confined structures where interfaces get closer in more than one dimension.

This calls for further studies on model systems, like arrays of lines, which are accessible to synchrotron radiation studies.

Conclusion

In this work the evolution of the kinetics of crystallization of Ge-rich GST (GGST) thin films is reported as a function of thickness in the range [5 nm -50 nm]. Thanks to X-ray synchrotron diffraction performed *in situ* during annealing, integrated intensity of Ge and GST diffraction peaks as well as peak breadth and position have been monitored as a function of time at different annealing temperatures. In accordance with previous works, we find that Ge crystallization precedes the one of GST. Ge and GST crystallization may be described with three time stages: (i) an incubation period; (ii) a fast growth period; (iii) a very slow growth period. Activation energies are reported for all the investigated films. A very high activation energy (between 3.6 and 4.3 eV) is reported for the incubation time t_0. In the case of Ge this incubation time is strongly thickness-dependent, which may have important consequences for the scaling of memories fabricated with this class of materials. The activation energy for the fast growth regime is close to the one reported for the crystallization of pure Ge films.

Supplementary Material

The Supplementary Material section contains additional figures where the integrated intensity for Ge **111**, Ge **220**, GST **200** and GST **220** is shown as a function of time at different annealing temperatures for a film thickness of 50 nm (Fig. S1), 25 nm (Fig. S2), and 10 nm (Fig. S3). Characteristic times t_1, t_2 and t_3 are shown in Arrhenius plots in figure S4 for the different film thickness and table S1 shows the corresponding activation energies. Figure S5 shows the influence of a temperature increase during isothermal anneal on the integrated intensity.

Acknowledgements

The authors gratefully acknowledge the SOLEIL Synchrotron for allocating beam time. P. Joly is acknowledged for excellent technical support during the experimental campaign at SOLEIL Synchrotron on DiffAbs beamline and Magali Putero is thanked for helping during some of the experiments. This research was supported by IPCEI/Nano 2022 program.

References

[1] M. Wuttig, & N. Yamada, Nature Mater. 6, 824 (2007).
[2] H.S.P. Wong, S. Raoux, S. Kim, J.L. Liang, J.P. Reifenberg, B. Rajendran, M. Asheghi, K.E. Goodson, Proc. IEEE 98, 2201 (2010).
[3] R.F. Freitas, W.W. Wilcke, IBM J. Res. Dev. 52 (2008) 439.
[4] G.W. Burr, B.N. Kurdi, J.C. Scott, C.H. Lam, K. Gopalakrishnan, R.S. Shenoy, IBM J. Res. Dev. 52 (2008) 449.
[4] D.J. Wouters, R. Waser, M. Wuttig, Proc. IEEE 103 (2015) 1274.
[5] A. Redaelli, A. Pirovano, A. Benvenuti, & A.L. Lacaita, J. Appl. Phys. 103, 111101 (2008).
[6] F. Pellizzer *et al*., 2004 Symposium on VLSI Technology, Digest of Technical Papers, Page18-19 (2004).
[7] P. Cappelletti, R. Annunziata, F. Arnaud, F. Disegni, A. Maurelli, P. Zuliani, J. Phys. D: Appl. Phys. 53, 193002 (2020).
[8] B. Legendre, C. Hancheng, S. Bordas and M.T. Clavaguera-Mora, Thermochim. Acta 78, 141 (1984).
[8] S. Bordas, M.T. Clavaguera-Mora, B. Legendre and C. Hancheng, Thermochim. Acta 107, 239 (1986).
[9] I. Friedrich, V. Weidenhof, W. Njoroge, P. Franz, M. Wuttig, J. Appl. Phys. 87, 4130 (2000).
[10] BS. Lee, JR. Abelson, SG. Bishop, DH. Kang, BK. Cheong, KB. Kim, J. Appl. Phys. 97, 093509 (2005).
[11] S. Privitera, E. Rimini, R. Zonca, Appl. Phys. Lett. 85, 3044 (2004).
[12] B.J. Kooi, W.M.G. Groot, J.T.M. De Hosson, J. Appl. Phys. 95, 924 (2004).
[13] I. I. Petrov, R.M. Imamov, & Z.G. Pinsker, Sov. Phys. Crystallogr. 13, 339 (1968)..
[14] T. Matsunaga, N. Yamada, Y. Kubota, Acta Crystallogr. Sect. B Struct. Sci. 60, 685 (2004).
[15] T. Nonaka, G. Ohbayashi, Y. Toriumi, Y. Mori, H. Hashimoto, Thin Solid Films 370, 258 (2000).
[16] N. Yamanda, E. Ohono, K. Nishiuchi, N. Akahira and M. Takao, J. Appl. Phys. 69, 2849 (1991).
[17] J. Park, M. R. Kim, W. S. Choi, H. Seo and C. Yeon, Jpn. J. Appl. Phys. 38, 4775 (1999).
[18] J. Orava, A. L. Greer, Acta Materialia 139, 226e235 (2017).
[19] J. Orava, A. L. Greer, B. Gholipour, D.W. Hewak and C. E. Smith, Nature Materials 11, 279 (2012).
[20] A. Aladool, M. M. Aziz, and C. D. Wright, J. Appl. Phys. 121, 224504 (2017).
[21] B. Chen, G. H. ten Brink, G. Palasantzas, and B. J. Kooi, J. Phys. Chem. C 121, 8569 (2017).
[22] N. Ciocchini, M. Cassinerio, D. Fugazza and D. Ielmini - IEEE Trans. on Electron Dev. 60, 3767 (2013).
[23] J. Zhao, J. Hui, Z. Ye, T. Lai, M. Y. Efremov, H. Wang, and L. H. Allen, Adv. Mater. Interfaces 9, 2200429 (2022).
[24] R. Anderson, J. Baglin, J. Dempsey, W. Hammer, F. d'Heurle, and S. Petersson, Appl. Phys. Lett. 35, 285 (1979).
[25] C.A. Angell, Science 267, 1924 (1995).
[26] HY. Cheng *et al*., 2011 IEEE International Electron Devices Meeting (IEDM), (2011).
[27] P. Zuliani *et al*., IEEE Trans Electron Devices 60, 4020 (2013).
[28] P. Zuliani, E. Palumbo, M. Borghi, G. Dalla Libera, R. Annunziata, Solid State Electron. 11, 27 (2015).

[29] F. Arnaud *et al.*, IEEE International Electron Devices Meeting IEDM, p. 24.2.1 (2020).
[30] A. Fantini, *et al.,* in 2010 International Electron Devices Meeting, 2010, 29.1.1–29.1.4.
[31] R. Fallica, E. Varesi, L. Fumagalli, S. Spadoni, M. Longo, C. Wiemer, Phys. Status Solidi (RRL) – Rapid Res. Lett. 7, 1107 (2013).
[32] T. Nirschl, et al., in 2007 IEEE International Electron Devices Meeting, 2007, pp. 461–464.
[33] Y. Yin, H. Zhang, S. Hosaka, Y. Liu, Q. Yu, J. Phys. D. Appl. Phys. 46, 505311 (2013).
[34] O. Thomas, C. Mocuta, M. Putero, MI. Richard, P. Boivin, F. Arnaud, Microel. Eng. 244-246, 111573 (2021)
[35] P. Hans, C. Mocuta, MI. Richard, D. Benoit, P. Boivin, Y. Le-Friec, R. Simola and O. Thomas, Phys. Status Solidi RRL 2100658 (2022).
[36] M. Agati *et al.*, J. Mater. Chem. C 7, 8720 (2019).
[37] E. Petroni *et al.,* Frontiers in Physics 10, 862954 (2022).
[38] https://www.synchrotron-soleil.fr/en/beamlines/diffabs
[39] K. Medjoubi, T. Bucaille, S. Hustache, J.-F. Bérar, N. Boudet, J-C. Clemens, P. Delpierre, & B. Dinkespiler, J. Synchrotron Rad. 17, 486 (2010).
[40] P. Pangaud, S. Basolo, N. Boudet, J.-F. Berar, B. Chantepie, P. Delpierre, B. Dinkespiler, S. Hustache, M. Menouni, & C. Morel, Nucl. Instrum. Methods Phys. Res. A 571, 321 (2007).
[41] K. Desjardins, C. Mocuta, A. Dawiec, S. Réguer, P. Joly, J.-M. Dubuisson, F. Alves, A. Noureddine, F. Bompard, D. Thiaudière, J. Synchrotron Rad. 29, 180 (2022).
[42] C. Mocuta, M.-I. Richard, J. Fouet, S. Stanescu, A. Barbier, C. Guichet, O. Thomas, S. Hustache, A. Zozulya, D. Thiaudière, J. Appl. Cryst. 46, 1842 (2013).
[43] M. Avrami, The Journal of Chemical Physics 7, 1103 (1939).
[44] M. Avrami, The Journal of Chemical Physics 8, 212 (1940).
[45] M. Avrami, The Journal of Chemical Physics 9, 177 (1941).
[46] W. A. Johnson, Am. Inst. Min. Metal. Petro. Eng. 135, 416 (1939).
[47] AN Kolmogorov, Bull. Acad. Sci. USSR, Math. Ser, (1937)
[48] M. A. Bab, L. A. Baum, and L. Mendoza-Zelis, Physica B, Condensed Matter 389, 193 (2007).
[49] M. J. Starink, Journal of Materials Science 32, 4061 (1997).
[50] M. J. Starink, Journal of Materials Science 36, 4433 (2001).
[51] G. V. M. Williams, A. Bittar, and H. J. Trodahl, J. Appl. Phys. 67, 1874 (1990).
[52] G. Garcia, A.F. Lopeandia, A. Bernardi, M.I. Alonso, A.R. Goni, J.L. Labar, J. Rodriguez-Viejo, J. of Nanosci. And Nanotechnol. 9, 3013 (2009).
[53] G.K. Krivyakin, V.A. Volodin, G.N. Kamaev, A.A. Popov, Semiconductors 54, 754 (2020).
[54] K. L. Chopra and S. K. Bahl, J. Appl. Phys. 40, 4171 (1969).
[55] Simone Raoux, Jean L. Jordan-Sweet, and Andrew J. Kellock, J. Appl. Phys. 103, 114310 (2008).
[56] X. Wei et al., Jap. J. Appl. Phys. 46, 2211 (2007).
[57] M. Zacharias and P. Streitenberger, Phys. Rev. B 62, 8391 (2000).
[58] E. Hüger, F. Staruss, J. Stahn, J. Deubener, M. Bruns, H. Schmidt, Sci. Rep. 8, 17607 (2018).
[59] N. Blum, C. Feldman, J. Non Cryst. Solids 22, 29 (1976).
[60] M.L. Theye, A. Gheorghiu, M. Gandais, S. Fisson, J. Non Cryst. Solids 37, 301 (1980).
[61] Y. Kwon and D-H Kang, Scripta Mat. 78-79, 29 (2014).

AIP Publishing

Journal of Applied Physics

PLEASE CITE THIS ARTICLE AS DOI: 10.1063/5.0157506

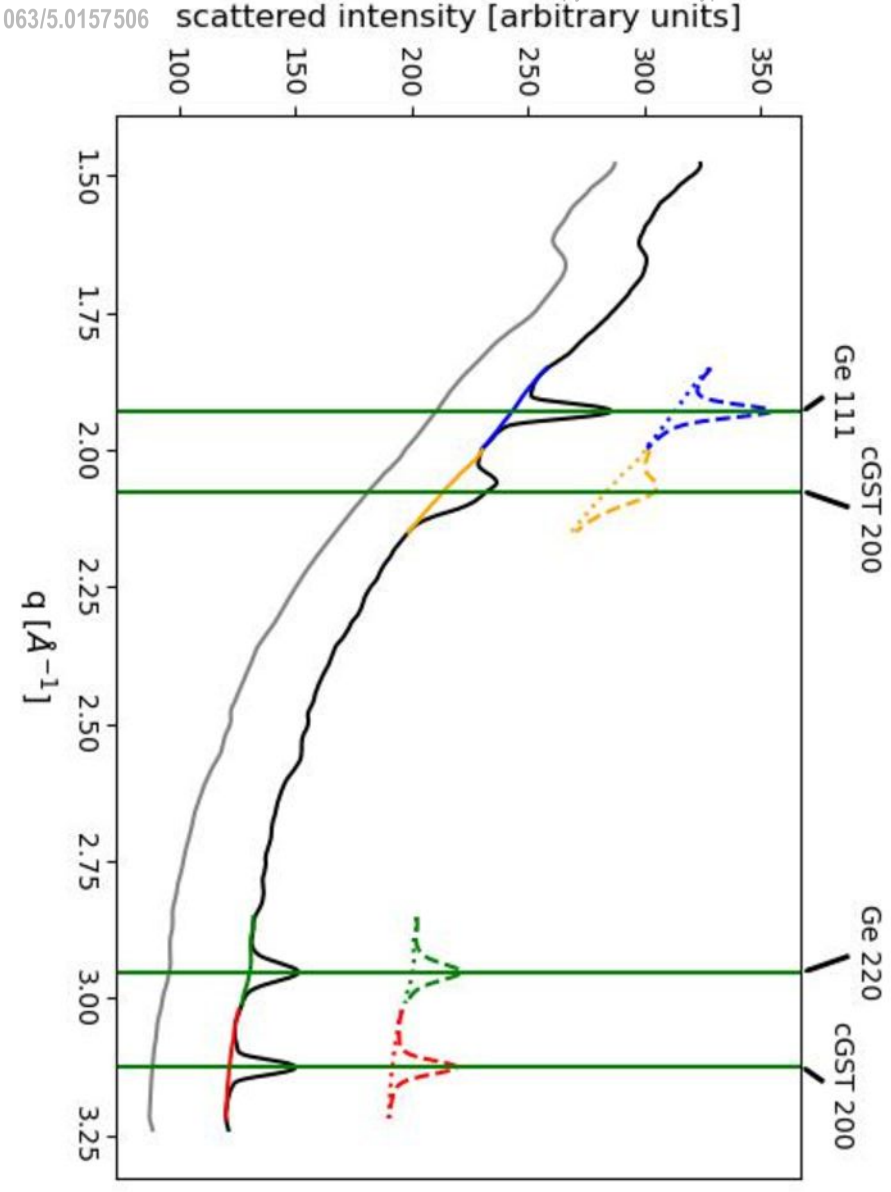

AIP Publishing

Journal of Applied Physics

PLEASE CITE THIS ARTICLE AS DOI: 10.1063/5.0157506

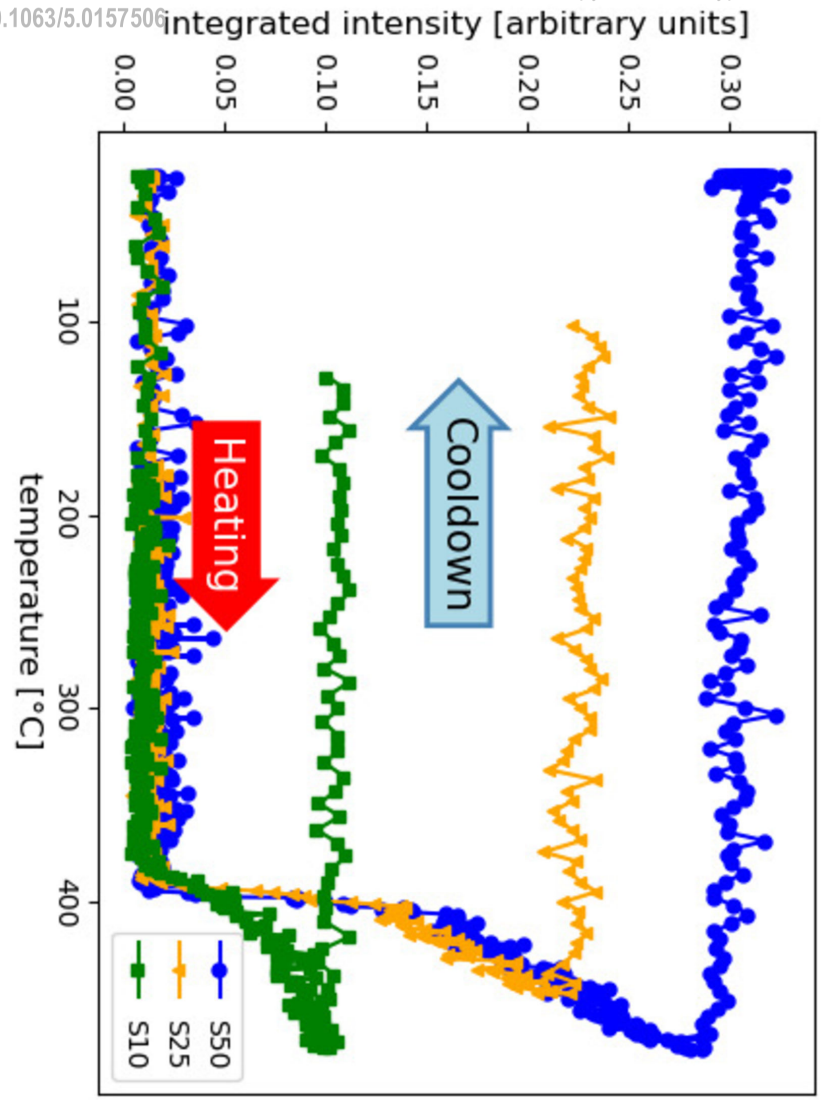

AIP Publishing

Journal of Applied Physics

PLEASE CITE THIS ARTICLE AS DOI: 10.1063/5.0157506

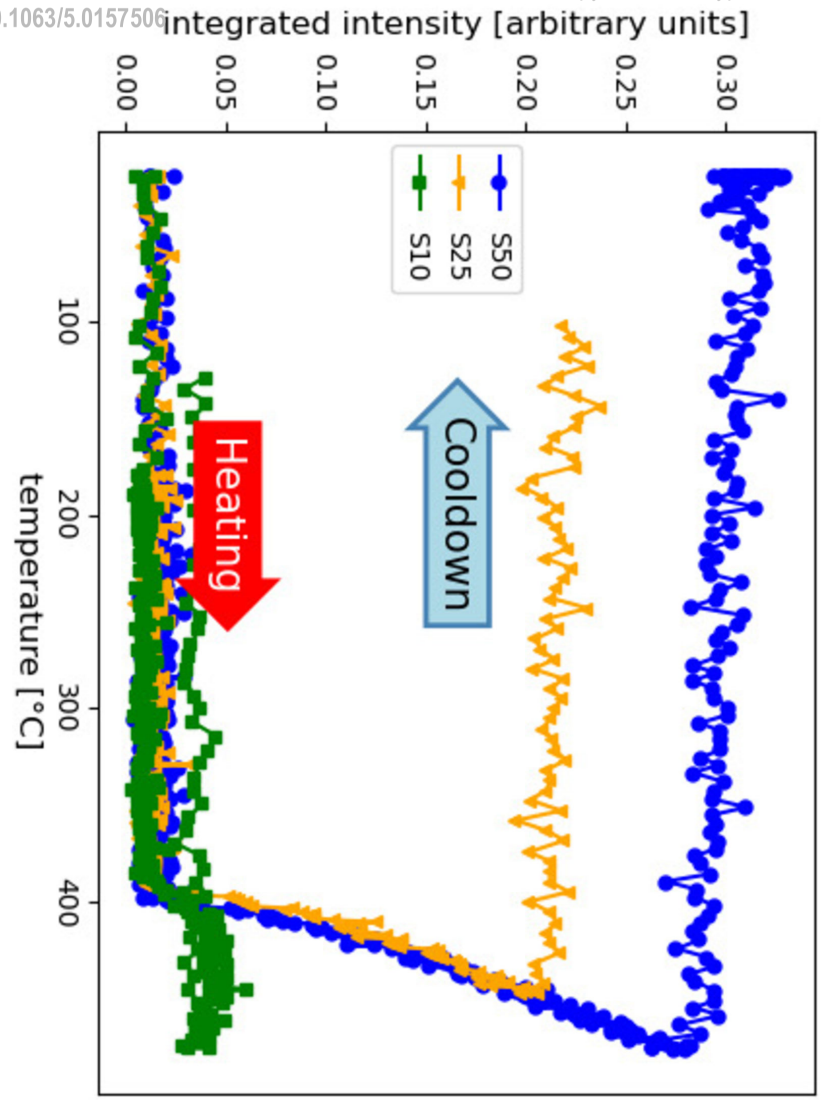

AIP Publishing

Journal of Applied Physics

PLEASE CITE THIS ARTICLE AS DOI: 10.1063/5.0157506

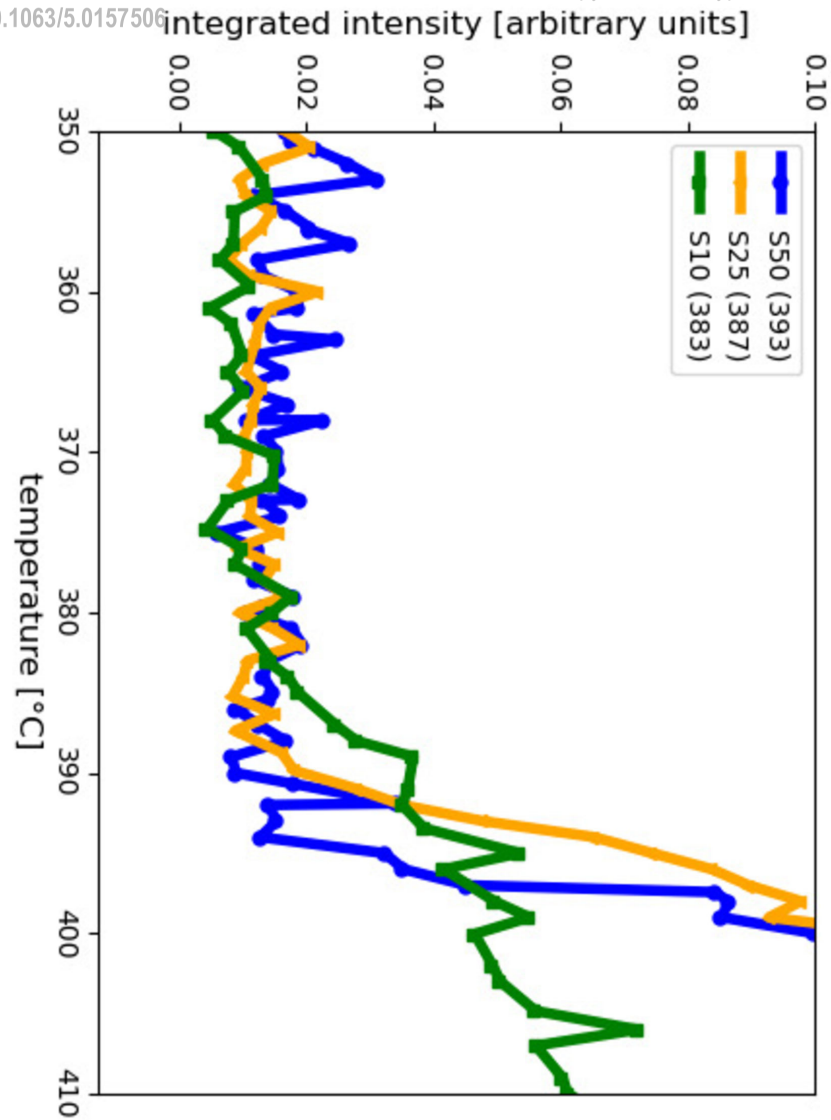

AIP Publishing

Journal of Applied Physics

PLEASE CITE THIS ARTICLE AS DOI: 10.1063/5.0157506

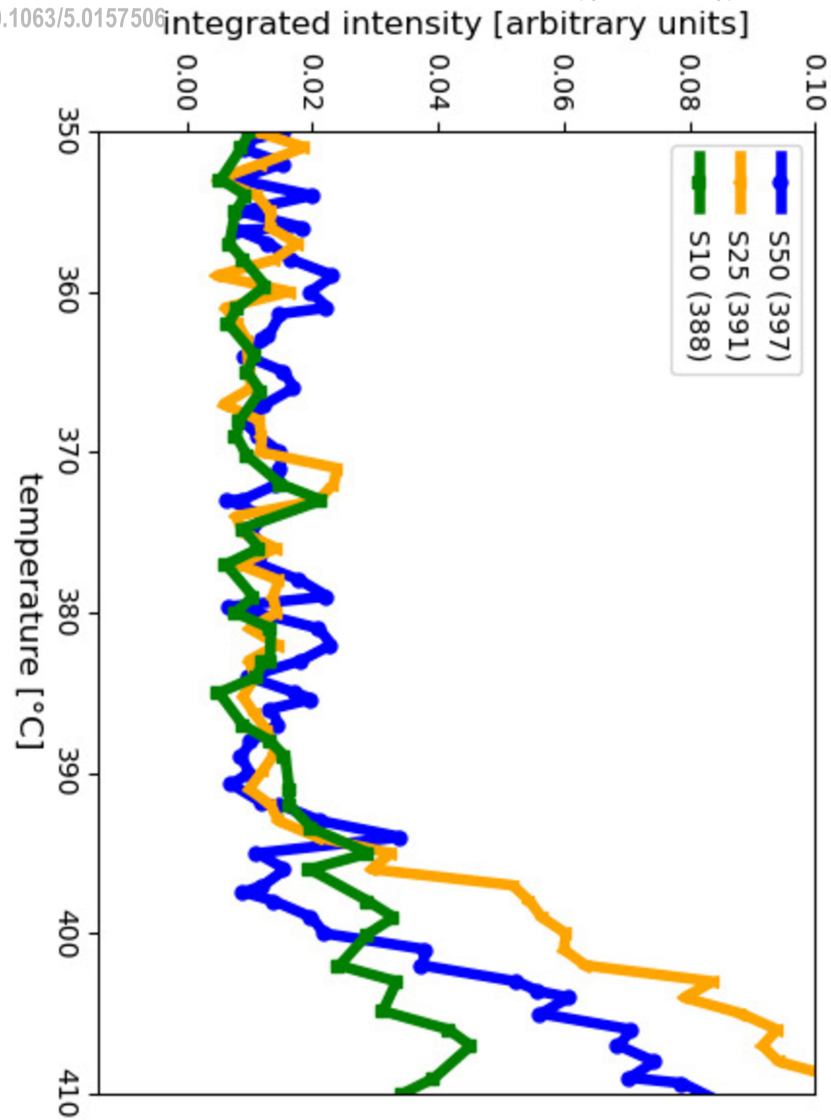

AIP Publishing

Journal of Applied Physics

ACCEPTED MANUSCRIPT

PLEASE CITE THIS ARTICLE AS DOI: 10.1063/5.0157506

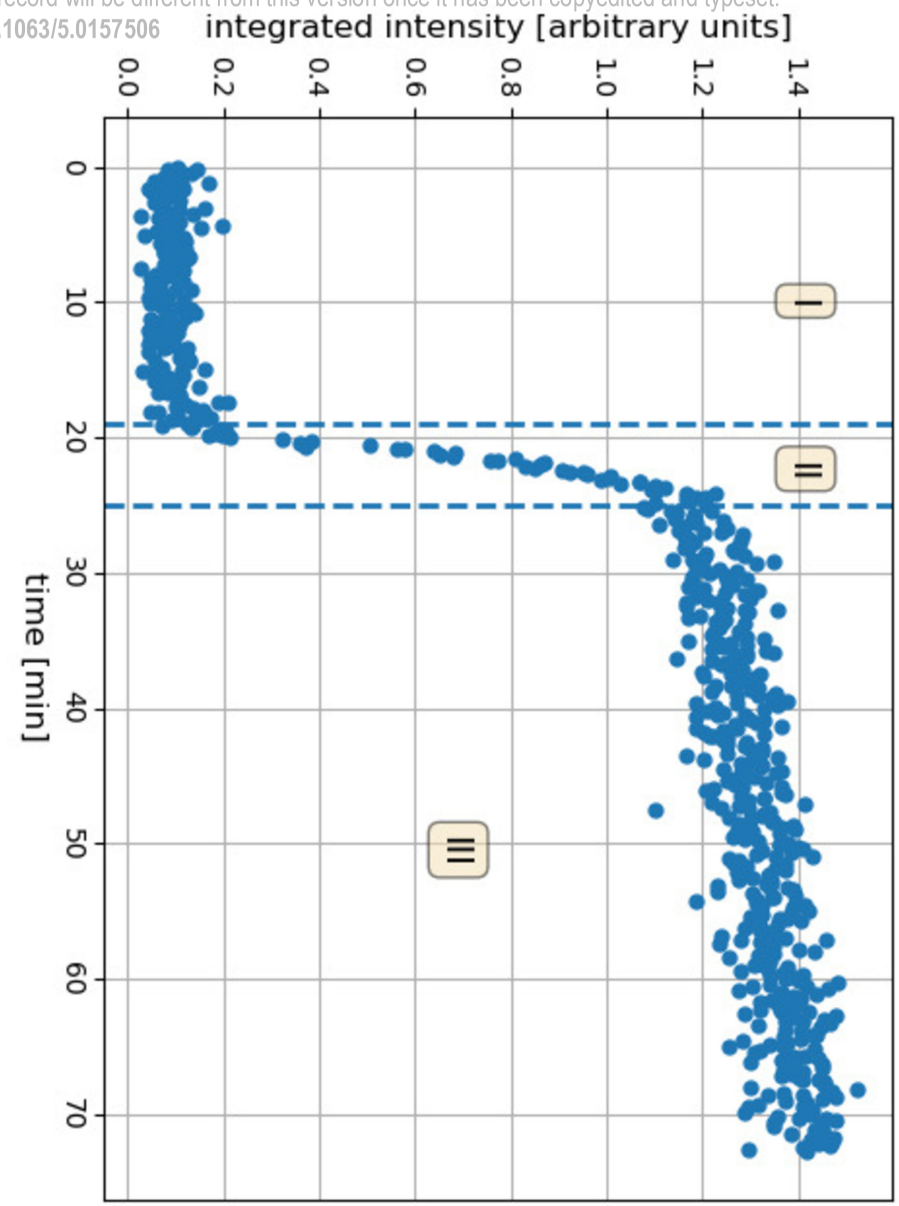

AIP Publishing

Journal of Applied Physics

ACCEPTED MANUSCRIPT

PLEASE CITE THIS ARTICLE AS DOI: 10.1063/5.0157506

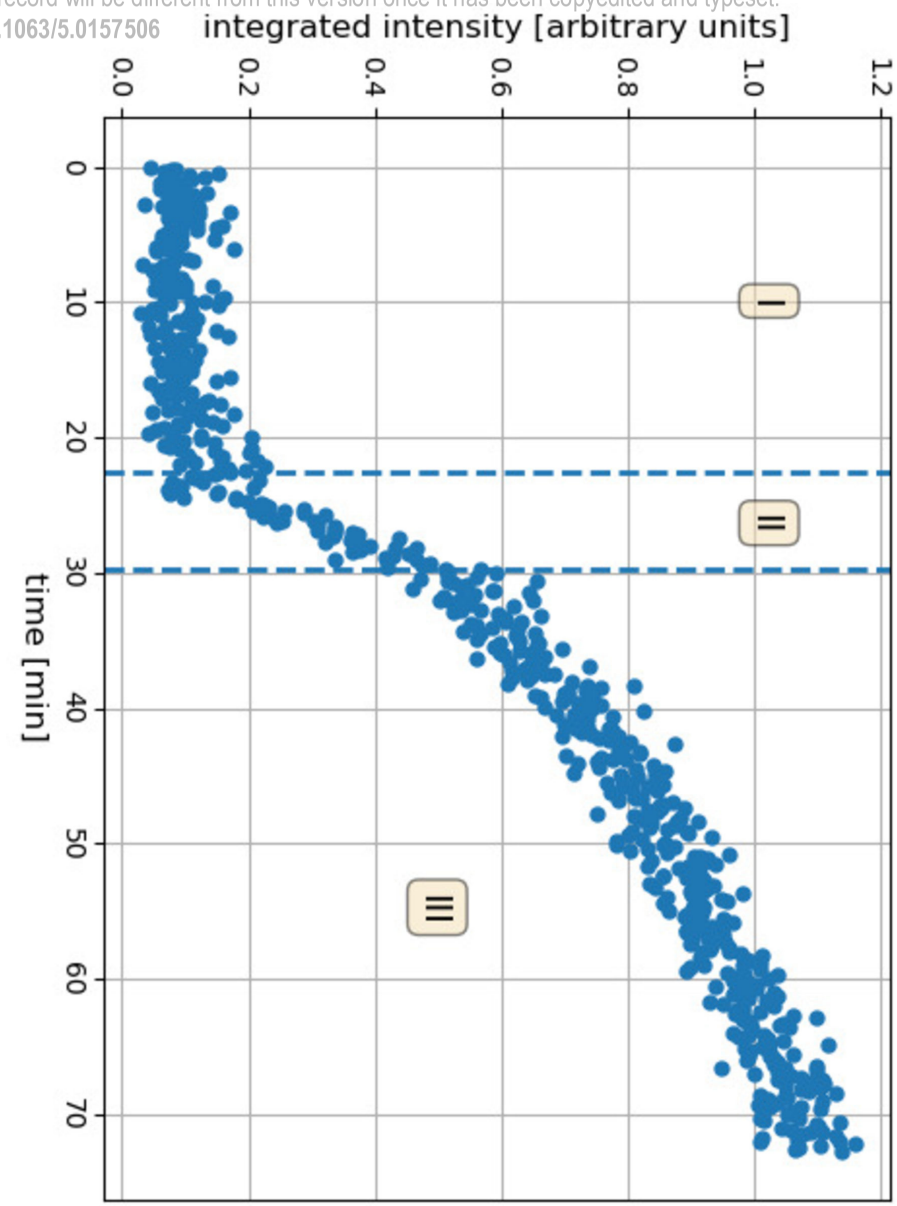

AIP Publishing

Journal of Applied Physics

PLEASE CITE THIS ARTICLE AS DOI: 10.1063/5.0157506

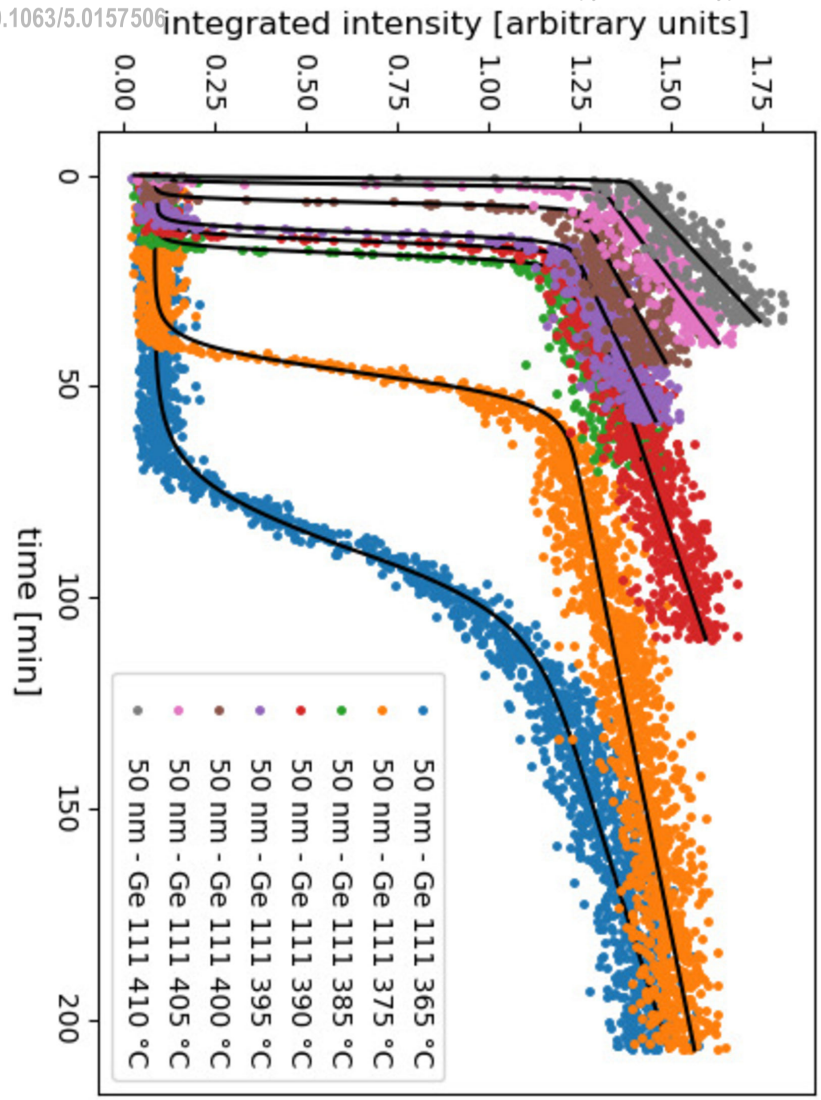

AIP Publishing

Journal of Applied Physics

PLEASE CITE THIS ARTICLE AS DOI: 10.1063/5.0157506

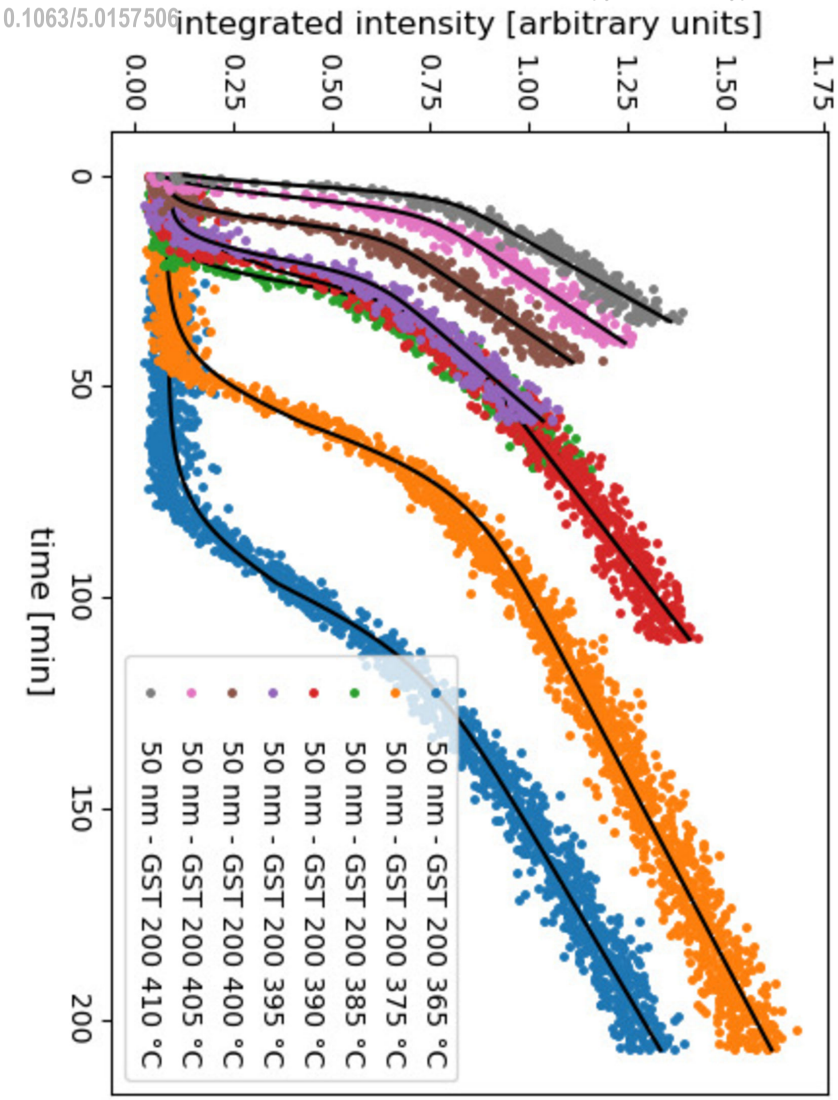

AIP Publishing

Journal of Applied Physics

PLEASE CITE THIS ARTICLE AS DOI: 10.1063/5.0157506

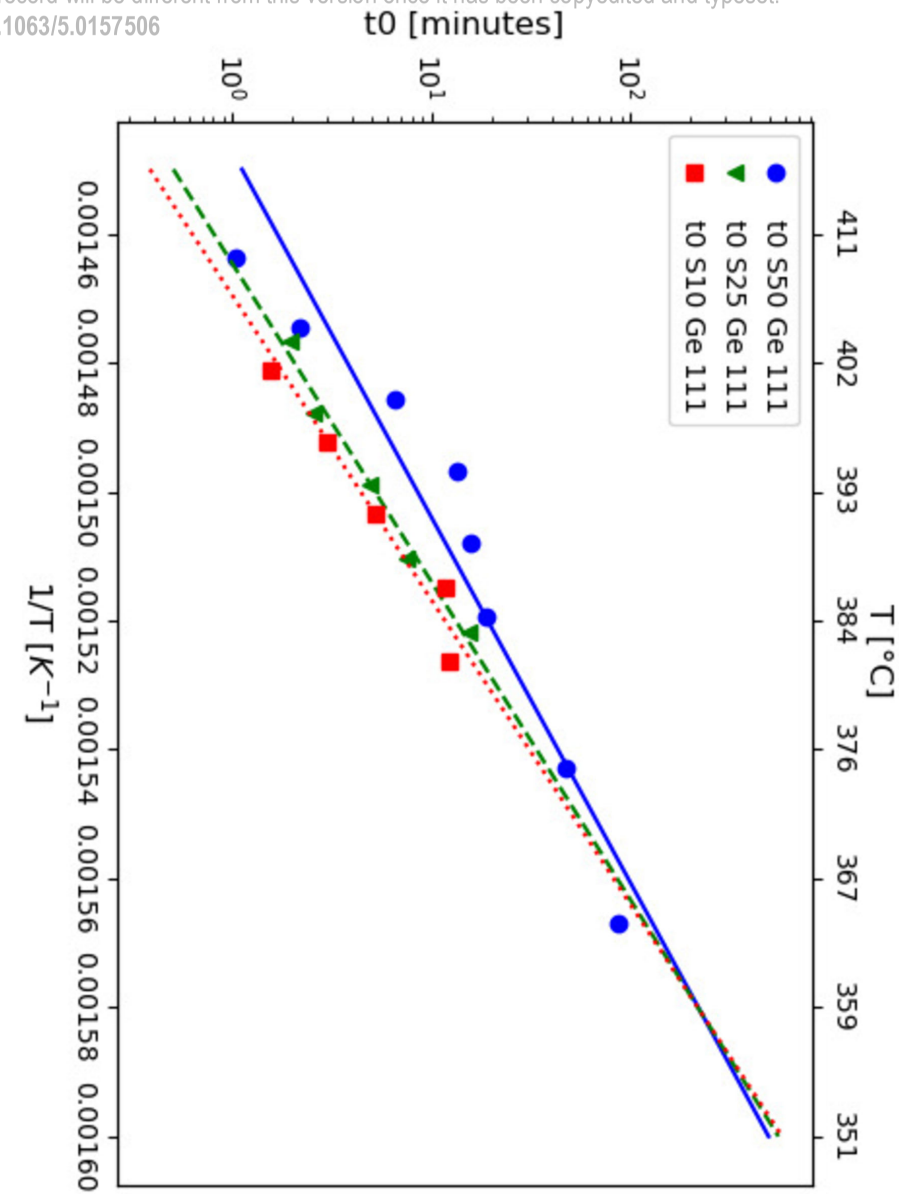

Journal of Applied Physics

AIP Publishing

Journal of Applied Physics

AIP Publishing

Journal of Applied Physics
AIP Publishing

AIP Publishing

Journal of Applied Physics

PLEASE CITE THIS ARTICLE AS DOI: 10.1063/5.0157506

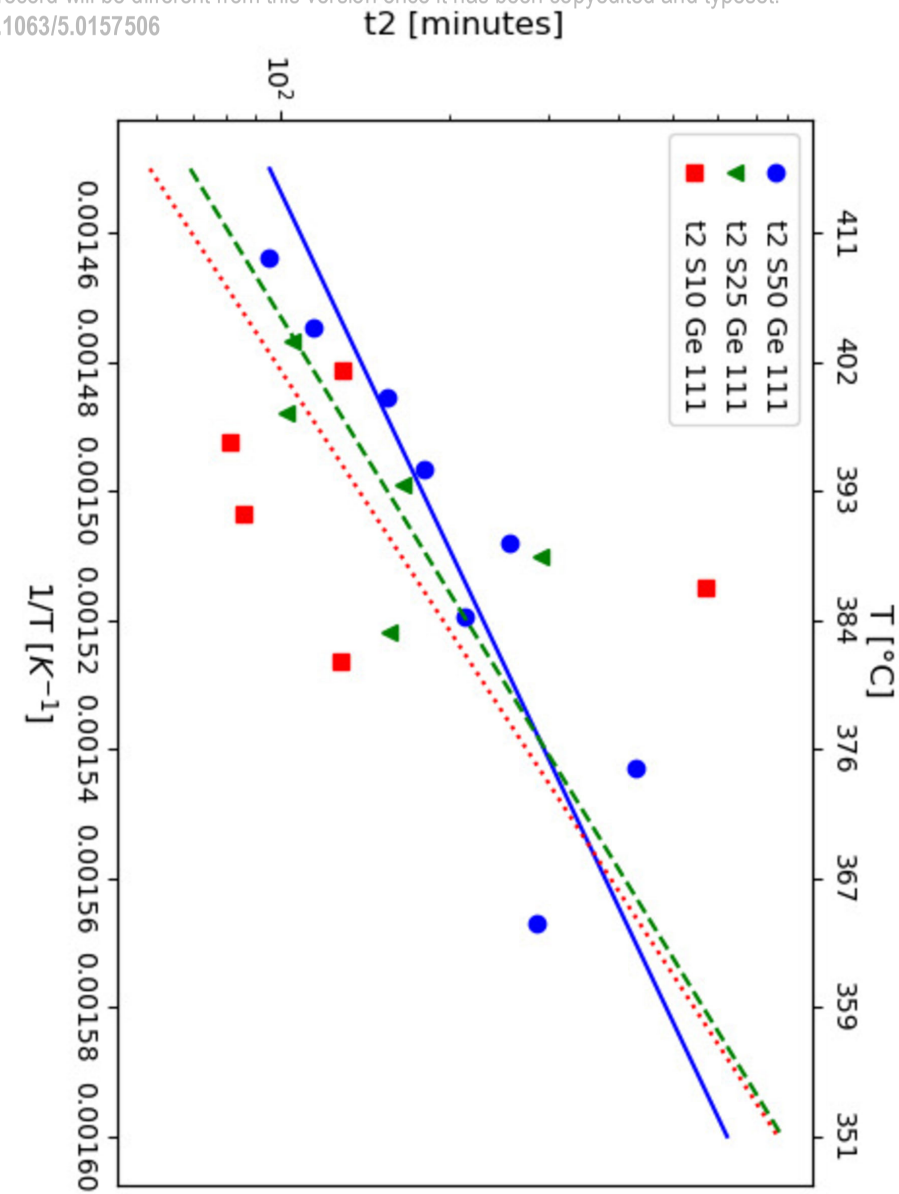

Journal of Applied Physics

AIP Publishing

AIP Publishing

Journal of Applied Physics

PLEASE CITE THIS ARTICLE AS DOI: 10.1063/5.0157506

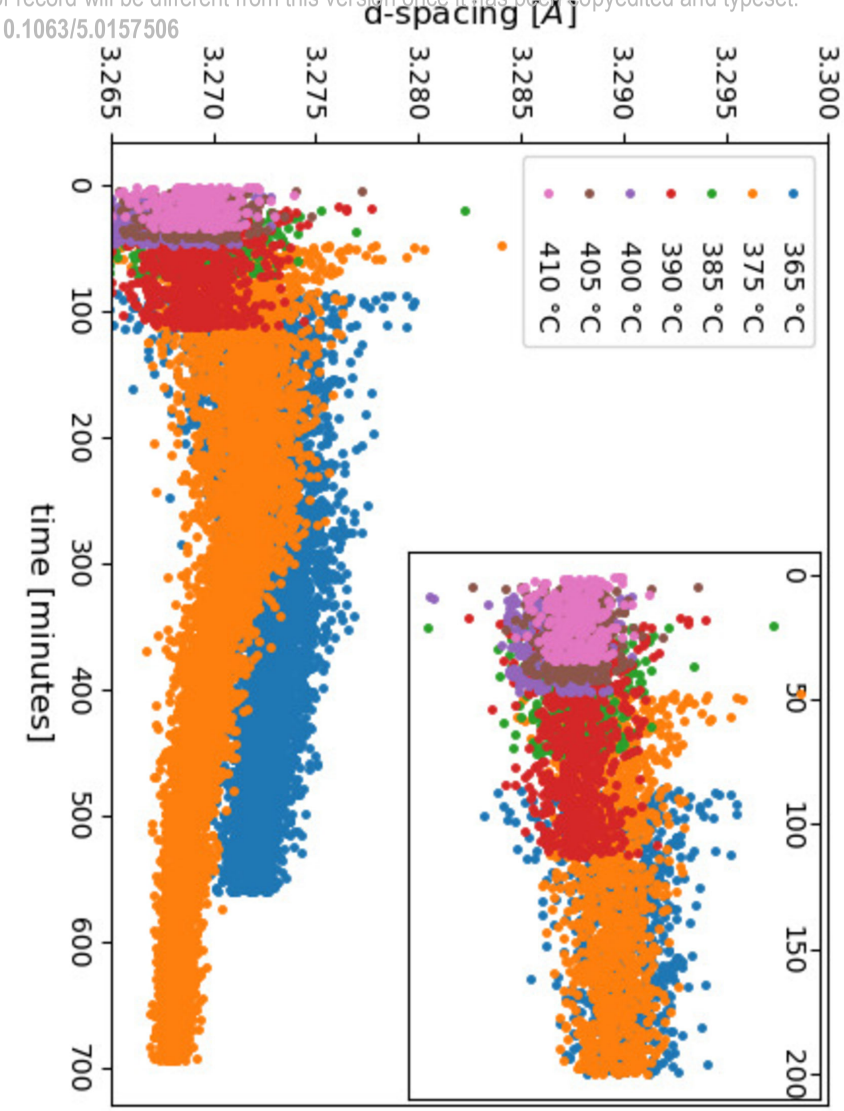

AIP Publishing

Journal of Applied Physics

PLEASE CITE THIS ARTICLE AS DOI: 10.1063/5.0157506

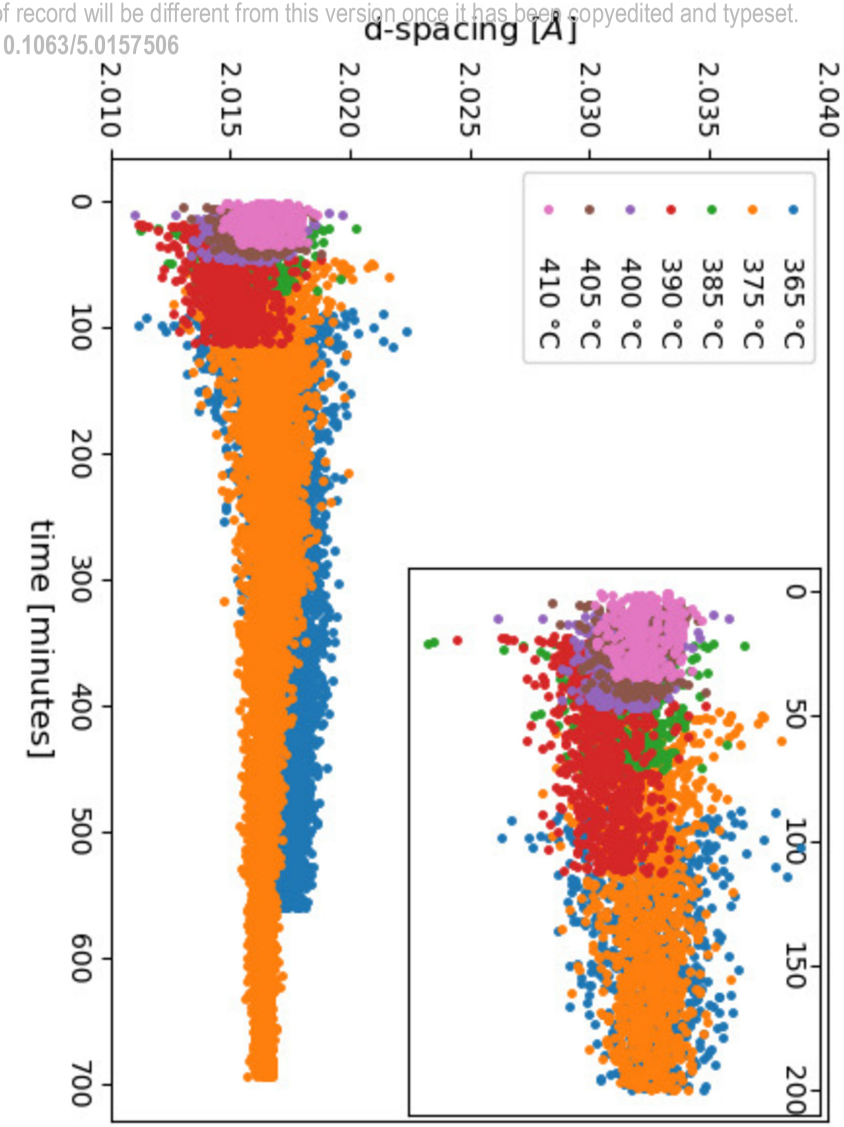

AIP Publishing

Journal of Applied Physics

PLEASE CITE THIS ARTICLE AS DOI: 10.1063/5.0157506

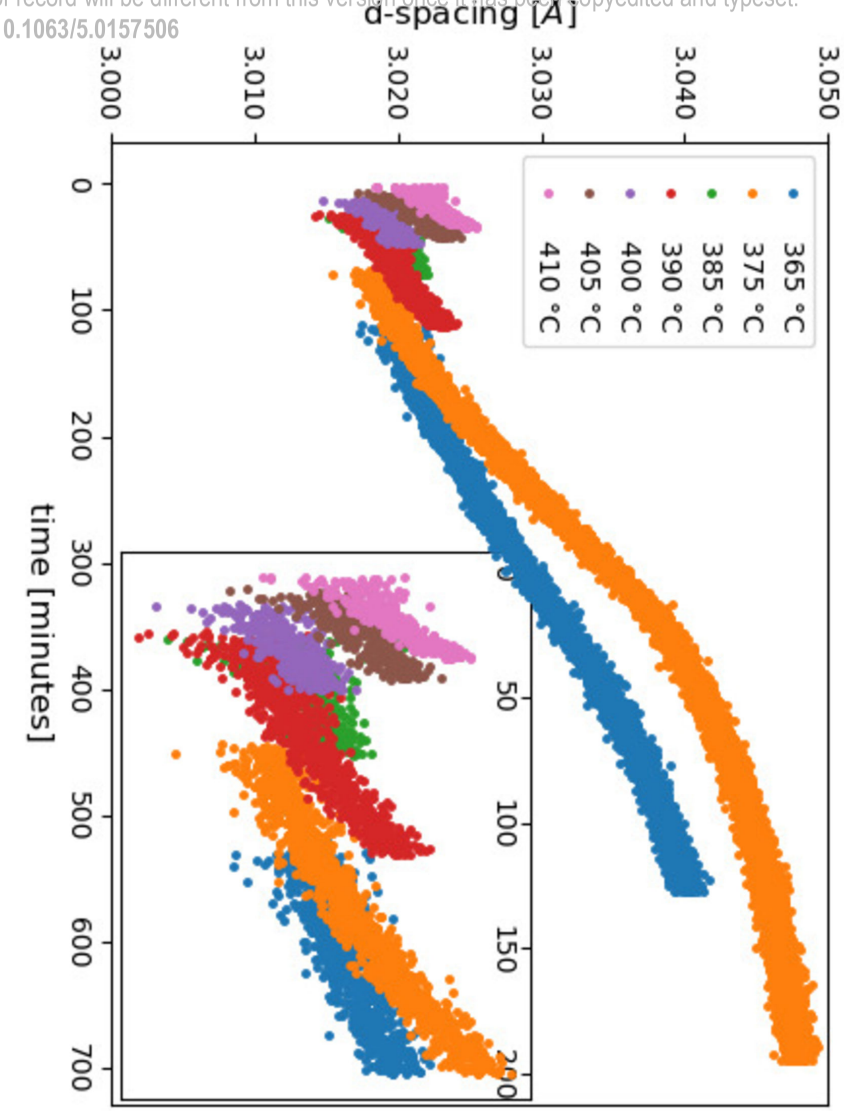

AIP Publishing

Journal of Applied Physics

PLEASE CITE THIS ARTICLE AS DOI: 10.1063/5.0157506

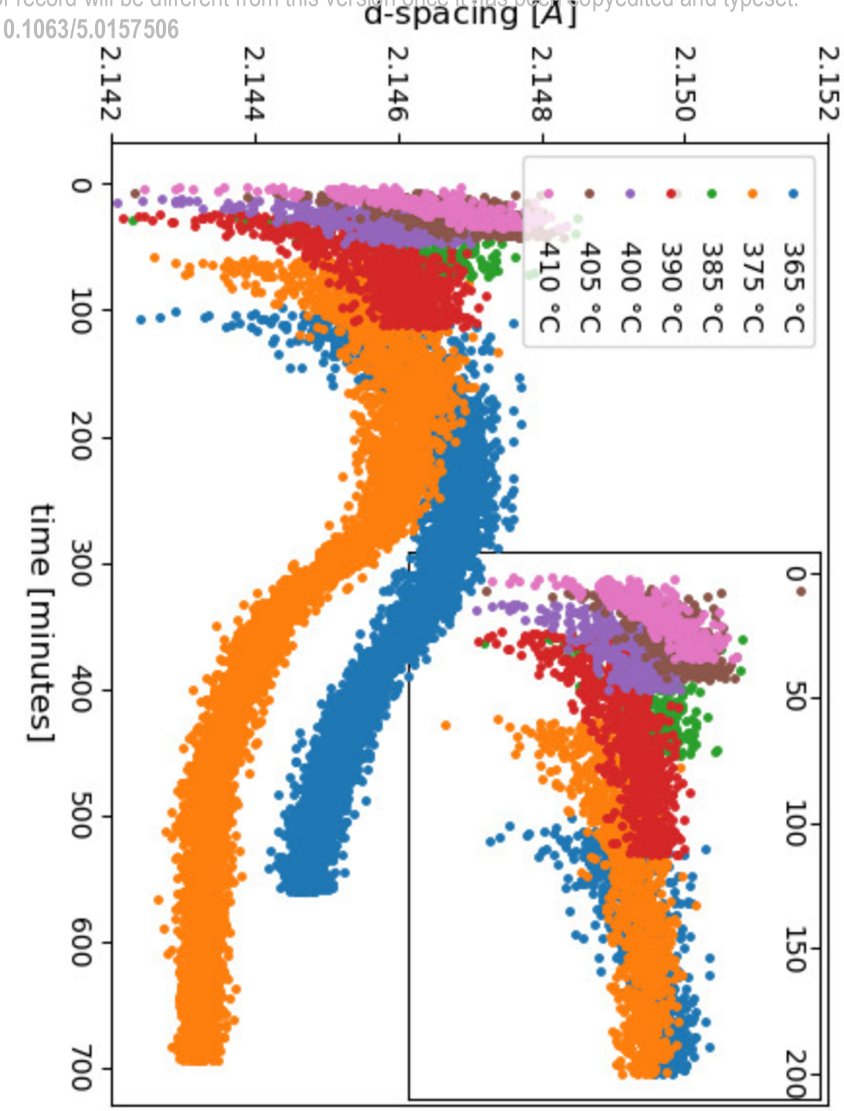

AIP Publishing

Journal of Applied Physics

PLEASE CITE THIS ARTICLE AS DOI: 10.1063/5.0157506

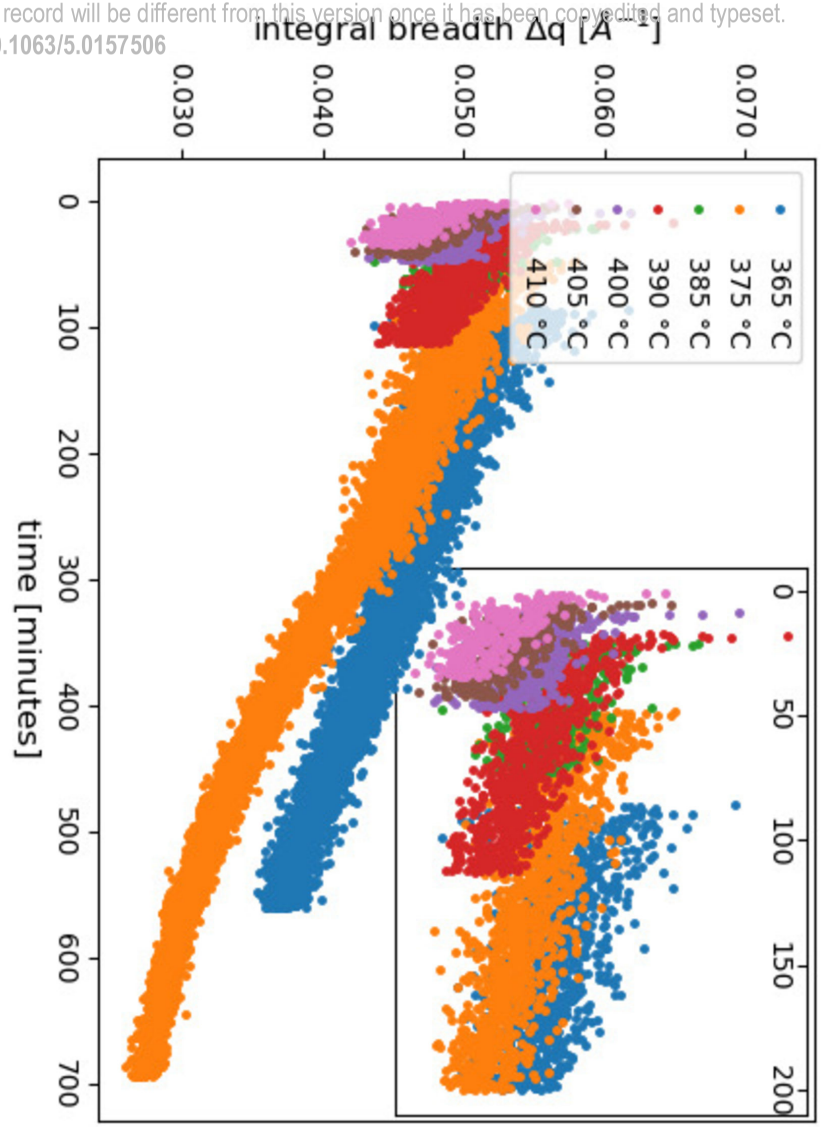

AIP Publishing

Journal of Applied Physics

PLEASE CITE THIS ARTICLE AS DOI: 10.1063/5.0157506

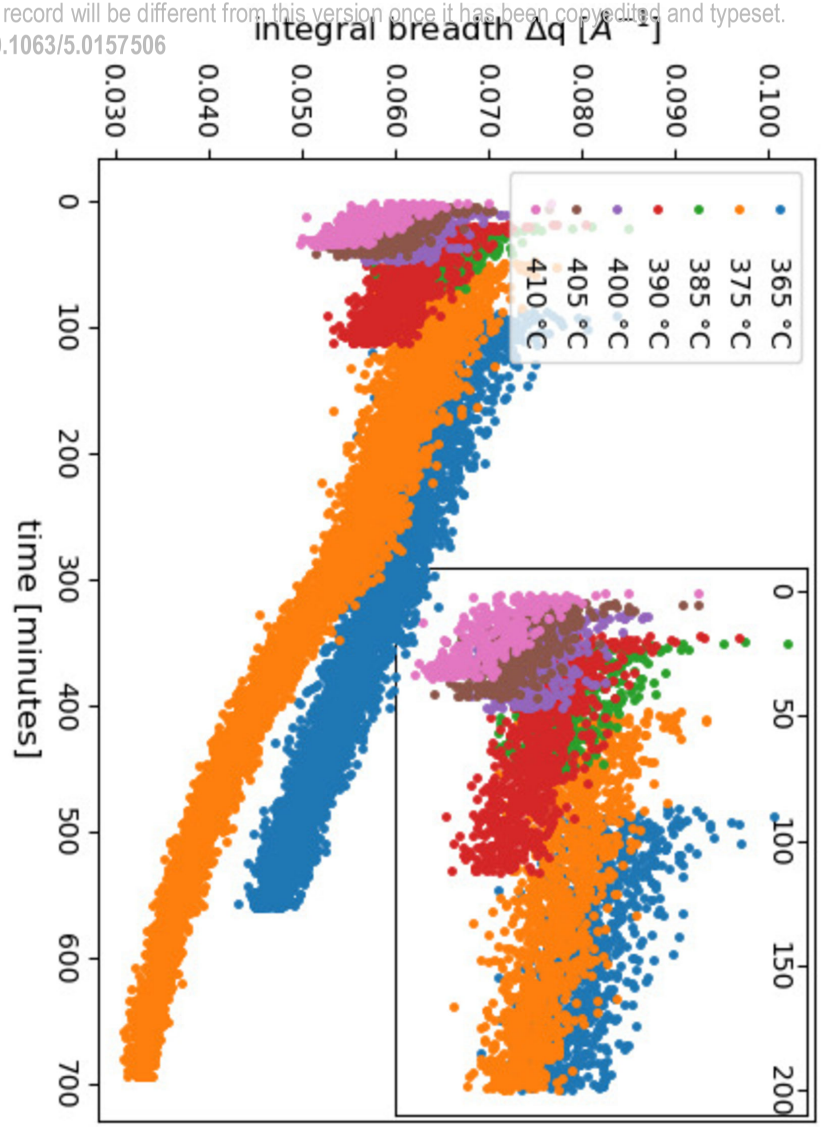

AIP Publishing

Journal of Applied Physics

PLEASE CITE THIS ARTICLE AS DOI: 10.1063/5.0157506

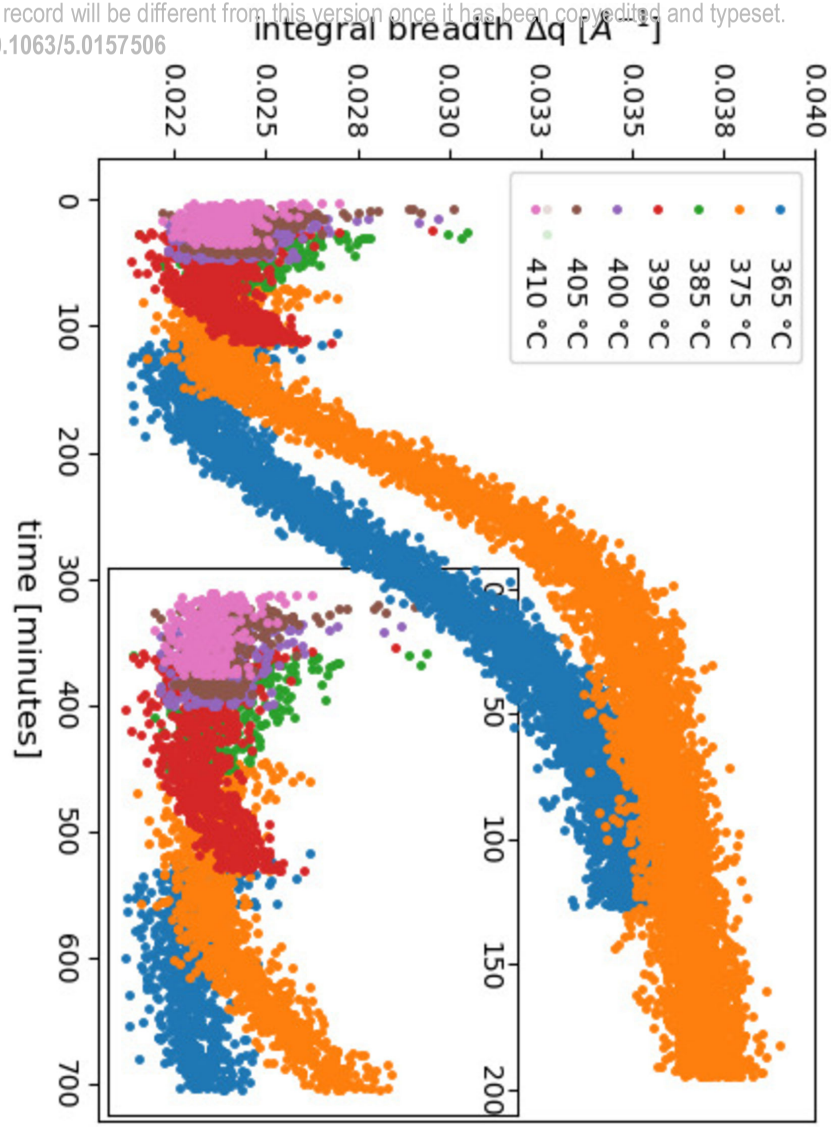

AIP Publishing

Journal of Applied Physics

PLEASE CITE THIS ARTICLE AS DOI: 10.1063/5.0157506

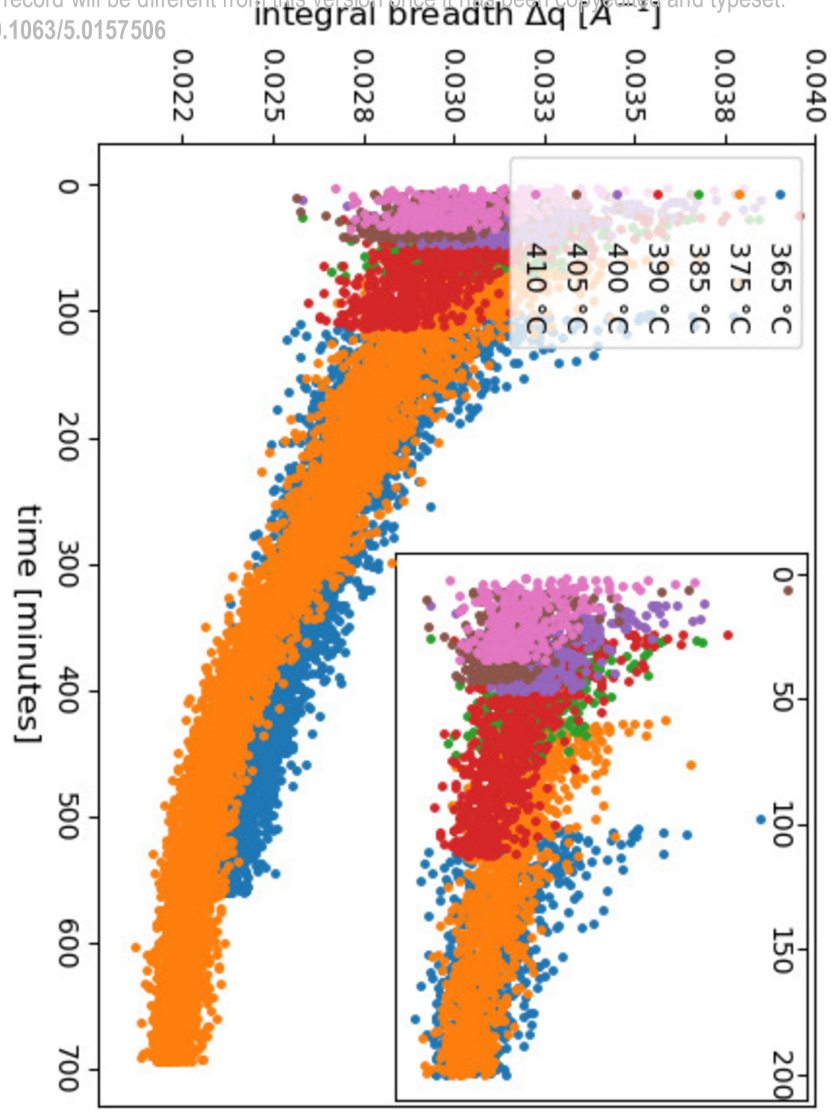

AIP Publishing

Journal of Applied Physics

PLEASE CITE THIS ARTICLE AS DOI: 10.1063/5.0157506

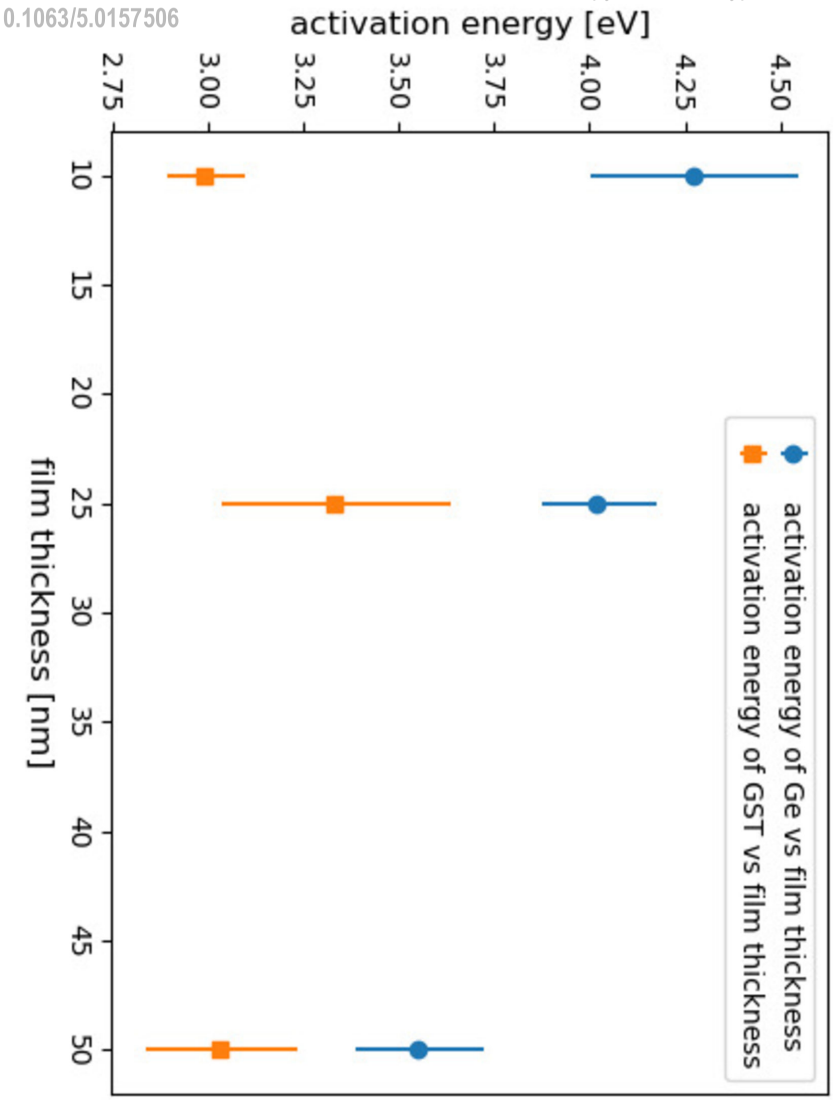

AIP Publishing

Journal of Applied Physics

ACCEPTED MANUSCRIPT

This is the author's peer reviewed, accepted manuscript. However, the online version of record will be different from this version once it has been copyedited and typeset.
PLEASE CITE THIS ARTICLE AS DOI: 10.1063/5.0157506